Journal of Fluids and Structures 133 (2025) 104232

Contents lists available at ScienceDirect

Journal of Fluids and Structures

journal homepage: www.elsevier.com/locate/jfs

A comprehensive numerical study on the current-induced fluid–structure interaction of flexible submerged vegetation

Inga Prüter [a,*], Felix Spröer [a], Kara Keimer [a], Oliver Lojek [a], Christian Windt [a], David Schürenkamp [a], Hans Bihs [b], Ioan Nistor [c], Nils Goseberg [a,d]

[a] *Leichtweiß-Institute for Hydraulic Engineering and Water Resources, Division of Hydromechanics, Coastal and Ocean Engineering, Technische Universität Braunschweig, Beethovenstraße 51A, Braunschweig, 38106, Germany*
[b] *Department of Civil and Environmental Engineering, Norwegian University of Science and Technology, Trondheim, 7491, Norway*
[c] *Department of Civil Engineering, University of Ottawa, 161 Louis Pasteur, Ottawa, ON K1N 6N5, Canada*
[d] *Coastal Research Center, Joint Central Institution of the Leibniz Universität Hannover and the Technische Universität Braunschweig, Merkurstraße 11, Hannover, 30419, Germany*

ARTICLE INFO

Keywords:
Fluid–structure interaction
Flexible vegetation
Large eddy simulation
REEF3D
Nature-based solutions

ABSTRACT

Submerged vegetation is becoming more and more relevant as a nature-based solution for coastal protection schemes, counteracting the effects of climate change and sea level rise. The numerical model REEF3D has been used to simulate the motion of and forces exerted on flexible vegetation under unidirectional currents. This study emphasizes the critical need for accurate solutions obtained by numerical models to investigate the complex ecosystem services, adopting a direct forcing approach using the immersed boundary method. The fluid–structure interaction capability within the finite difference model is comprehensively evaluated for the simulation of stem motions and forces exerted on flexible vegetation under varying unidirectional flows. Thresholds for numerical parameters, including a minimum number of 25 rigid elements composing the stem, are identified for accurate solutions. The necessity of using large eddy simulations and a Smagorinsky constant of 0.1 to simulate the turbulent flow is demonstrated. The study confirms the accuracy of the implemented fluid–structure interaction model to replicate stem bending (less than 10 % deviation relative to the stem length) and forces across varying hydrodynamic conditions.

1. Introduction

Vegetation such as seagrass or salt marsh species are flexible structures that are either permanently or temporarily submerged in coastal waters and therefore exposed to hydrodynamic forces by waves and tidal currents. Vegetation is commonly considered an ecosystem engineer along the coastal rims (Ondiviela et al., 2014; Himes-Cornell et al., 2018; Marin-Diaz et al., 2023). The ecosystem service capacity of coastal vegetation includes wave attenuation, sediment accumulation, and soil stabilization (King and Lester, 1995; Anderson and Smith, 2014; Rupprecht et al., 2017), which provides beneficial and supportive capabilities for coastal zone management to counteract the predicted sea level rise (Vuik et al., 2019). The complex ecosystem services and non-linear interactions between flexible submerged vegetation and fluids drive the need for the development of state-of-the-art numerical

---

[*] Corresponding author.

E-mail addresses: inga.prueter@tu-braunschweig.de (I. Prüter), felix.sproeer@tu-braunschweig.de (F. Spröer), k.keimer@tu-braunschweig.de (K. Keimer), o.lojek@tu-braunschweig.de (O. Lojek), c.windt@tu-braunschweig.de (C. Windt), d.schuerenkamp@tu-braunschweig.de (D. Schürenkamp), hans.bihs@ntnu.no (H. Bihs), inistor@uottawa.ca (I. Nistor), n.goseberg@tu-braunschweig.de (N. Goseberg).

https://doi.org/10.1016/j.jfluidstructs.2024.104232
Received 25 January 2024; Received in revised form 13 October 2024; Accepted 24 November 2024

methods that accurately approximate their hydrodynamic response. The characteristics of the interaction between the fluid's velocity and pressure fields with the elastically-flexing vegetation depend on the material and geometrical properties of the vegetation (Liu et al., 2021), as well as on the magnitude of the hydrodynamic forces (Bouma et al., 2005); this interplay is commonly known as fluid–structure interaction (FSI).

Nowadays it can be considered state of the art to represent the vegetation in the FSI as a flexible body. On the process level, it is straightforward to agree that the flexibility of plant motion reduces the frontal area of the plant and the relative velocity between the plant and the water, as the flexible structure bends, resulting in a motion instigated by the hydrodynamic loading (van Veelen et al., 2020). The resulting reconfiguration of plants due to external loading can be either classified as *avoidance strategy* (minimum frontal area) or as *tolerance strategy* (maximized resistance to breakage), see Puijalon et al. (2011). Vegetation that is classified to follow the avoidance strategy has a lower flexural stiffness. The importance of including plant flexibility in studies has been shown, for example, in the analysis of the ability of vegetation to dampen incoming waves, whose wave energy reduces with increasing flexibility by 30 % to 70 % depending on the study (Mullarney and Henderson, 2010; van Veelen et al., 2020).

Two main approaches can be found in the literature to model the FSI numerically. Some methods employ semi-empirical formulations to include forces, such as drag and buoyancy, into the force balance. The specific formulations applied in the force balance of different numerical models vary, depending on the complexity of the model, e.g. by considering skin friction (Dijkstra and Uittenbogaard, 2010; Zhu et al., 2020). With the semi-empirical approach, the drag forces are calculated using the Morison equation, as performed in the works of Dijkstra and Uittenbogaard (2010), Mullarney and Henderson (2010), Maza et al. (2013) and Jin and Zhang (2022). In each of these studies, the Morison equation contains specific values of the drag coefficient (C_D). The dependency of C_D on the Reynolds number (Re) has been frequently investigated (Losada et al., 2016; van Veelen et al., 2020), but plant flexibility was usually not taken into account. While Whittaker et al. (2015) have incorporated the plant flexibility into the calculation of the drag force, values for C_D are still required. Values of C_D for specific plant species, especially regarding seasonal variation obtained from field measurements, e.g. Keimer et al. (2023, 2024), are scarce and render more accurate modeling attempts futile. A uniform drag coefficient for flexible vegetation might not exist (van Veelen et al., 2020) and is therefore of limited applicability for numerical models (van Veelen et al., 2020; Caroppi and Järvelä, 2022). The present study argues that simplistic approaches requiring coefficients like C_D cannot accurately simulate the FSI with flexible vegetation and are not further considered in this study. Accurately incorporating the variability of flexible vegetation using drag coefficients requires extensive field and laboratory investigations to generate a widely applicable dataset, considering the different vegetation species, stem–leaf configurations unaddressed so far, seasonality, and biomechanical variations within a stem.

A second, more versatile approach for numerical FSI involves direct forcing. Although this method promises higher accuracy, it does not inherently guarantee improved results, as replicating the complex geometry of live vegetation remains challenging. Direct forcing requires some form of coupling between the fluid and structural solvers. One way of achieving such coupling is to include both the fluid and the structural solver in a Lagrangian model such as the smoothed-particle hydrodynamics (SPH) approach, as shown in O'Connor and Rogers (2021) for DualSPHysics. Alternatively, el Rahi et al. (2023) proposed recently the coupling of a Lagrangian fluid approach in DualSPHysics with an external finite element method (FEM) solver. Another possibility is the coupling of an Eulerian approach for the fluid with a Lagrangian approach for the structural solver. To achieve such coupling, the Eulerian grid needs to be able to communicate with the Lagrangian grid of the structural solver and vice versa. To facilitate the communication between the two systems, a body-fitted mesh can be applied, for example, using the arbitrary Lagrangian-Eulerian (ALE) method which ensures a strong coupling. A recent implementation using a body-fitted grid was presented by Chourdakis et al. (2023). Body-fitted meshes have the drawback of mesh deformations and re-meshing when large deformations of the structural solver occur, requiring thus high computational power. Chourdakis et al. (2023) described numerical problems using OpenFOAM for simulations when the deformed mesh led to distorted cells, requiring advanced mesh motion techniques.

Alternatively, the immersed boundary method (IBM) has become increasingly popular. An Eulerian structural solver can be implemented via the IBM into the Lagrangian fluid phase, as shown by Tian et al. (2014), Tschisgale and Fröhlich (2020) Wang et al. (2020), He et al. (2022), Wang et al. (2022), Ni et al. (2023), Kim et al. (2024), Hagmeyer et al. (2024) and Agrawal et al. (2024). The IBM has the advantage of accounting for large deformations of the structural solver with an Eulerian grid and a stable fluid solver with a Lagrangian grid. The achieved accuracy of FSI studies using the IBM is promising, rendering it the favored coupling method within the context of this study. Although the previously mentioned works are all based on the IBM, they differ through their proposed coupling algorithm of the FSI, as well as the applied fluid and structural solver. He et al. (2022) applied an inextensible nonlinear Euler–Bernoulli beam, with the bending motion restricted to the streamwise–vertical direction. Similarly, Ni et al. (2023) simulated in two dimensions to focus on the monami modes of a flexible vegetation meadow. Hagmeyer et al. (2024) proposed a strongly coupled partitioned solution algorithm to model a torsion-free beam. Alternatively, Kim et al. (2024) used a finite-element structural solver with soft-body dynamics, while Wang et al. (2020) used a structural solver based on the combined finite element method–discrete element method. Both Tschisgale and Fröhlich (2020) and Agrawal et al. (2024) used the geometrically exact Cosserat rod for their structural solver, which has the advantage of capturing three-dimensional motion while using a mathematical model in one direction, thus making it computationally more efficient. Additionally, Agrawal et al. (2024) were able to simulate coarser structural meshes than the background fluid grid, highlighting the potential of such a model.

Flexible vegetation usually induces turbulent flow conditions, which can numerically either be achieved with direct numerical simulation (DNS) or via turbulence modeling. To date, DNS still comes at comparatively high computational costs when higher Reynolds numbers are concerned. The k-ϵ turbulence model in the Reynolds-averaged Navier–Stokes (RANS)-approach was often extended to include vegetation-induced turbulence to account for flexible vegetation (Dijkstra and Uittenbogaard, 2010; Maza et al., 2013; Chen and Zou, 2019). Turbulence modeling with large eddy simulations (LES) additionally resolves some of the larger scale eddies in the flow, while the smaller portion of the energy cascade is modeled with a semi-empirical approach, known as the subgrid scale (SGS) model. Widely used SGS models are the Smagorinsky model (Tschisgale and Fröhlich, 2020; Kim et al., 2024) and the wall-adapting local eddy-viscosity (WALE) model (Ouro and Stoesser, 2017). A dynamic Smagorinsky model has been used by Mattis et al. (2015), Wang et al. (2022) and He et al. (2022) to investigate flexible vegetation. In recent years, Tschisgale and Fröhlich (2020) implemented a Cosserat rod method into a fluid solver. They chose a Smagorinsky constant $C_S = 0.15$ for their SGS, based on similar values in the literature (0.15 and 0.17) for flexible vegetation. Building on their previous study, Tschisgale et al. (2021) compared varying values of C_S (0.075, 0.15, 0.30) for a flexible meadow without finding significant differences in the velocity profile and the resolved turbulent shear stress. To the authors' knowledge, no further literature discussed which C_S would be suitable to model flexible vegetation. Further evaluation is required to quantify the extent of the contribution of the SGS constant like the Smagorinsky coefficient C_S or the WALE-coefficient C_W to accurately resolve the turbulence of the flow field around the flexible vegetation.

For an accurate representation of the complex FSI that is presented when flexible stems bend because of fluid forces, this study proposes a two-way coupling based on the IBM, along with specific turbulence modeling via RANS or LES. In line with the set requirements, this work chooses an implementation of a structural solver (Tschisgale and Fröhlich, 2020) implemented in the numerical model REEF3D::CFD, which is a finite difference (FD) incompressible, two-phase fluid solver including turbulence models common in computational fluid dynamics (CFD) codes. Another structural solver including flexibility has already been validated in REEF3D for mooring lines, which are represented in a one-way coupling fashion (Martin and Bihs, 2021). Although the structural solver calculates the forces acting on the solid directly, damping coefficients (see Section 2.1) are required to take the non-linear viscous damping of rods into account (Linn and Lang, 2013). Martin and Bihs (2021) observed that their model was not sensitive to the damping coefficients in steady-state conditions as long as they differed from zero, ensuring numerical stability. Nevertheless, these coefficients influence the transient stem motion, as observed by Martin and Bihs (2021) for the minimum and maximum tension force of a swinging elastic rod.

This study tests the FSI of stems representing aquatic vegetation under currents. Several studies in literature (Tian et al., 2014; Tschisgale and Fröhlich, 2020; Jin and Zhang, 2022) validated their model based on the current experiments of a single stem as an approximation of a plant stem by Luhar and Nepf (2011). The pertinent literature often addressed the FSI problem on either a single type of material or a single stem length. While it is important to demonstrate that numerical models can approximately govern this type of FSI problem methodically in the first place, this study aims to widen the scope of this problem to a broader range of both material properties and stem lengths; aside from these material and geometrical properties, it will be very important for further studies, i.e., on sediment transport, to better understand the effect of a wider range of hydraulic loading conditions, from very low to high exposure of the stem to the fluid motion. As this is the first study to investigate the application of the structural solver in REEF3D::CFD for flexible vegetation, the sensitivity of the model regarding parameters like the number of elements of the stem needs to be tested. From the literature, it becomes clear that different turbulence models have been applied to simulate flexible vegetation in the past. Yet, it remains open which turbulence model is suitable to accurately simulate the FSI in the FD CFD solver used for this study. Insufficient information is available regarding the application of the damping coefficient in the context of FSI with flexible vegetation and its possible relation to material properties. That relation could be crucial once field data of vegetation is implemented in the model and to accurately simulate the stem motion under waves in future studies. In summary, the following specific objectives will be addressed within this study:

- To test the model sensitivity, including its temporal and spatial resolution, to numerical parameters of the structural solver, such as the number of elements of a stem.
- To investigate the effect of different turbulence models and their model parameters on the resulting drag force exerted on single, flexible stems.
- To compare the model predictions regarding different materials, varying stem lengths, and current velocities to physical (Luhar and Nepf, 2011) and numerical (Tschisgale and Fröhlich, 2020) results.
- To evaluate the influence of the damping coefficients under uniform current loads on the resulting forces and their further implications.

2. Methodology

2.1. Numerical model

The employed numerical model is the FD solver REEF3D::CFD, characterized by the level-set method to describe the free surface and its high-order discretization schemes. The fluid solver is based on the incompressible Navier–Stokes equations, i.e., the continuity equation (1) and the incompressible momentum equation (2).

$$\frac{\partial u_i}{\partial x_i} = 0 \tag{1}$$

$$\frac{\partial u_i}{\partial t} + u_j \frac{\partial u_i}{\partial x_j} = -\frac{1}{\rho_f}\frac{\partial p}{\partial x_i} + \frac{\partial}{\partial x_j}\left[(\nu + \nu_t)\left(\frac{\partial u_i}{\partial x_j} + \frac{\partial u_j}{\partial x_i}\right)\right] + g_i \tag{2}$$

In Eqs. (1) and (2), u_i denotes the velocity vector in three dimensions (x, y, z), t is the time component, ρ_f is the density of the fluid, g is the gravitational acceleration, and the pressure p. Two viscosity components are included, with ν corresponding to the fluid

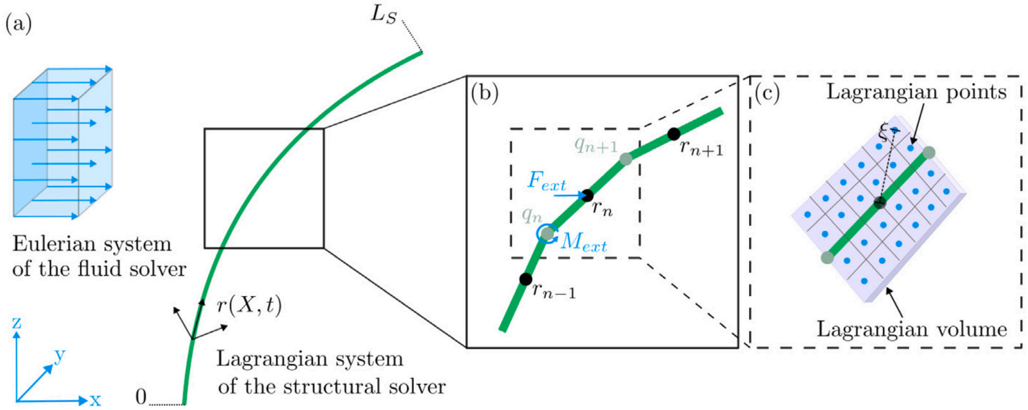

Fig. 1. Definition sketch of the coupling of the structural and the fluid solver (adapted after Tschisgale and Fröhlich (2020), Martin and Bihs (2021)) with (a) the Eulerian and Lagrangian system, (b) the external forces (F_{ext}) and moments (M_{ext}) calculated for each element center (r_n) and element edge (q_n) and (c) the Lagrangian points of an individual element, where the velocity components of the fluid are transferred, with the vector ξ representing the distance of the Lagrangian points to each element's center (r_n).

molecular kinematic viscosity. The eddy viscosity ν_t accounts for the Reynolds stress term using RANS equations and can be solved with models, e.g., the k-ω model, as described in Bihs et al. (2016). RANS formulations require particular attention when accounting for sharp velocity gradients or unsteady flow fields (Bush et al., 2019). These potential instabilities can generally be mitigated by applying limiters to the eddy viscosity across the entire fluid domain, as used in Unsteady Reynolds-averaged Navier–Stokes (URANS) methods, or by adapting the turbulence production in the proximity of the stem. The latter is here enabled by implementing a new formulation accounting for increased turbulent energy dissipation along the stem. Following the logarithmic law of the wall, the turbulent energy dissipation ω is enhanced at the surface of the stem by calculating its modification ω^* as follows

$$\omega^* = \frac{C_T D(\max(0,k))^{0.5}}{1/3(\delta x + \delta y + \delta z)\kappa C_\mu^{0.25}} \tag{3}$$

including a turbulence factor, applied here with $C_T = 50$, the kernel function D locating the grid points at the surface of the stem, the turbulent kinetic energy k, the local cell size $(\delta x, \delta y, \delta z)$ and turbulence model constants κ, here equal to 0.4, and C_μ, here equal to 0.09. The implications of this first approach to account for the FSI using the k-ω model are presented in Section 3.1.

Alternatively, a spatially filtered Navier–Stokes equation can be applied to solve the subgrid-scale eddy viscosity for the LES equations. The solver can either model the subgrid-scale eddy viscosity by the Smagorinsky model or the WALE model. In the Smagorinsky model, eddies smaller than the length scale $\Delta = \sqrt[3]{\partial x \partial y \partial z}$ are not resolved but instead modeled based on the Smagorinsky subgrid-scale model:

$$\tau_{ij} - \frac{1}{3}\tau_{kk}S_{ij} = \nu_t\left(\frac{\partial \bar{u}_i}{\partial x_j} + \frac{\partial \bar{u}_j}{\partial x_i}\right) = 2\nu_t \bar{S}_{ij}, \tag{4}$$

including the subgrid-scale stress $\tau_{ij} = \overline{u_i u_j} - \bar{u}_i\bar{u}_j$ and the sub-grid scale eddy viscosity of the large scale field $\nu_t = C_S^2\Delta^2|\bar{S}|$ with the strain rate $|\bar{S}| = (\bar{S}_{ij}\bar{S}_{ij})^{\frac{1}{2}}$. For more details on the implementation and validation, the reader is referred to Bihs et al. (2016). The WALE model, proposed by Nicoud and Ducros (1999), accounts for the rotational rate of the strain rate tensor in contrast to the Smagorinsky model, which generally reduces to zero close to walls.

The structural solver is based on the geometrically exact Cosserat rod equations (Lang et al., 2011; Tschisgale and Fröhlich, 2020). The implementation of the flexible structure in the fluid solver via IBM consists of the Eulerian coordinates of the fluid solver (x-, y-, and z-direction) and the Lagrangian coordinates (X) of the structural solver (Fig. 1a). The flexible structure itself is divided into n individual, rigid elements (see Fig. 1b). The forces and moments are calculated for each individual, rigid element. The coupling of the two coordinate systems is achieved via the Lagrangian points at the surface of the Lagrangian volume, depicted in Fig. 1c, where the velocity components of the fluid are transferred. Hereby, each marker point represents a Lagrangian volume, which must be smaller or equal to the size of the Eulerian fluid cell to ensure the impermeability of the structural solver. The distance of the Lagrangian points to each element's center is determined by the vector ξ.

The two geometrically exact Cosserat rod equations are detailed in Eqs. (5) and (6). Eq. (5) describes the translational motion $r(X,t)$ by calculating the acceleration of the rod's centerline, for each Lagrangian coordinate $X \in [0; L]$. The rotational motion $R(X,t)$ of the rod is calculated by Eq. (6).

$$\rho_s A \ddot{\underline{r}} = \frac{\partial \underline{f}}{\partial X} + \underline{f}_{\text{ext}} \tag{5}$$

$$\rho_s \underline{I}\dot{\underline{\omega}} + \underline{\omega} \times \rho_s \underline{I}\underline{\omega} = \frac{\partial \underline{m}}{\partial X} + \frac{\partial \underline{r}}{\partial X} \times \underline{f} + \underline{m}_{\text{ext}} \tag{6}$$

In Eqs. (5) and (6), ρ_s, A, and I represent constant material parameters, i.e., the density of the solid, the area of the cross-section, and the second moment of area, respectively. While $\underline{f}$ and $\underline{m}$ describe the internal force and moment of the rod, $\underline{f}_{\text{ext}}$ and $\underline{m}_{\text{ext}}$ determine the external force and moment. The internal force $\underline{f}$ due to shearing and stretching and the internal moment $\underline{m}$ due to bending and twisting are determined for a linear viscoelastic material of Kelvin–Voigt type (Martin and Bihs, 2021; Tschisgale and Fröhlich, 2020):

$$\underline{f} = R\,\underline{f}_0 = R\,C_{\varepsilon,0} \cdot (R^T \underline{\varepsilon} - (R^T \underline{\varepsilon})|_{\mathrm{t=0}}) + R\,C_{\dot{\varepsilon},0} \cdot (\dot{R}^T \underline{\varepsilon} - (R^T \underline{\dot{\varepsilon}})) \tag{7}$$

$$\underline{m} = R\,\underline{m}_0 = R\,C_{\kappa,0} \cdot (R^T \underline{\kappa} - (R^T \underline{\kappa})|_{\mathrm{t=0}}) + R\,C_{\dot{\kappa},0} \cdot (\dot{R}^T \underline{\kappa} - (R^T \underline{\dot{\kappa}})) \tag{8}$$

Both equations are the sum of the linear elastic part (first addend) and the dissipative part due to internal friction (second addend) and include the strain ($\underline{\varepsilon} = \frac{\partial \underline{r}}{\partial X}$) and curvature ($[\underline{\kappa}]_x = \frac{\partial R}{\partial X}$) vector. The shearing ($C_{\varepsilon,0}$) and bending ($C_{\kappa,0}$) stiffness used in Eqs. (7) and (8) depend on the material properties and are respectively determined by the following diagonals:

$$C_{\varepsilon,0} = \mathrm{diag}(EA,\ c_{\mathrm{s,Y}}GA,\ c_{\mathrm{s,Z}}GA) \tag{9}$$

$$C_{\kappa,0} = \mathrm{diag}(c_{\mathrm{t}}GI_X,\ EI_Y,\ EI_Z) \tag{10}$$

In both Eqs. (9) and (10), E corresponds to the Young's modulus and G to the shear modulus. I_Y and I_Z correspond to the second moment of area and $I_X = I_Y + I_Z$ to the second polar moment of area. The coefficients $c_{\mathrm{s,Y}}$, $c_{\mathrm{s,Z}}$, and c_{t} are shear and torsion correction factors to account for warping effects for shear and torsional load (Tschisgale and Fröhlich, 2020). That warping effect is not considered within this study and therefore set equal to unity. Correction factors for generic cross-sections are given in Freund and Karakoç (2016). Symbols $C_{\dot{\varepsilon},0}$ and $C_{\dot{\kappa},0}$ are both diagonals that account for the structural viscosity. The first is for translational damping, the latter for rotational damping. The diagonals can be expressed as follows:

$$C_{\dot{\varepsilon},0} = \mathrm{diag}(c_{\mathrm{dx}}, c_{\mathrm{dy}}, c_{\mathrm{dz}}) \tag{11}$$

$$C_{\dot{\kappa},0} = \mathrm{diag}(c_{\mathrm{kx}}, c_{\mathrm{ky}}, c_{\mathrm{kz}}) \tag{12}$$

Herein, c_{dx} accounts for the axial extension or compression, while c_{dy} and c_{dz} dampen the shear force. In the same manner, c_{kx} accounts for torsion, while c_{ky} and c_{kz} dampen the bending moment. Further information can be obtained in Lang et al. (2011) and Linn and Lang (2013).

The external force in Eq. 4 is the sum of the gravitational force ($f_g = (\rho_s - \rho_f)Ag$) and the coupling force f_Γ of the immersed boundary. The spatial coupling of f_Γ, which accounts for the difference between the three-dimensional shape of the immersed boundary to the one-dimensional Cosserat rod, is achieved by connecting the Lagrangian marker points to the Eulerian grid cells, cf. Fig. 1c, via regularized delta functions. Ensuring faster communication, the velocity field of the fluid is then replaced by the integral quantity $\tilde{p}_e$ for the force and $\tilde{l}_e$ for the moment, reducing the communication points to six for each rod element. The temporal coupling of f_Γ for the direct forcing approach is achieved through five steps, using an implicit Runge–Kutta scheme. First, a preliminary velocity is calculated for the next time level without considering the immersed boundary, which is communicated to the structural solver in the second step. In a third step, the interface velocity of the next time level is obtained using the coupling force f_Γ for each element

$$f_{\Gamma,\mathrm{e}} \Delta Z = - \left[\frac{p_\Gamma - p_\Gamma^{r-1}}{t - t^{r-1}} + \frac{p_\Gamma^{r-1} - \tilde{p}}{2\alpha_r \Delta t} \right]_e , \tag{13}$$

with the linear momentum of the fluid layer around an element $p_{\Gamma,\mathrm{e}}$, the preliminary linear momentum $\tilde{p}_e$ obtained in the first step and α_r as a coefficient of the Runge–Kutta scheme. Afterward, the coupling force at the current time level can be calculated based on the difference between the preliminary and calculated velocity. Finally, the velocity field of the next time level can be calculated in the fifth step, based on the resulting coupling force of step number four. Further specifications and the analog determination of the external momentum can be found in Tschisgale and Fröhlich (2020).

2.2. Model set-up

This work concerns fluid flow loading on a flexible stem resulting from uniform currents. The structural solver is first employed to test the response of a stem in currents based on the experimental work by Luhar and Nepf (2011), further referred to as the reference experiment, whereby both the bending motion and the drag force are compared. Additionally, high-resolution photos and the measured forces have been provided by Luhar and Nepf (2011). The flow field is compared to the numerical simulations of Tschisgale and Fröhlich (2020), who provided their simulation data, enabling a direct comparison of the results. Finally, measured plant properties from the field are applied to the structural solver to provide a first approximation of the capabilities of the proposed model. The plant properties from the field are taken from the study by Keimer et al. (2023), which defined different growth states of the salt marsh plant *Spartina anglica*.

Several stem lengths (0.05 m to 0.25 m) exposed to varying current velocities (0.04 m/s to 0.32 m/s) have been tested in the reference experiment. The current velocities were measured with a variation smaller than 5 % with an acoustic Doppler velocimeter placed in front of the stem. Measured average forces are available for all configurations, with the resolution of the load cell of 0.001 N and accuracy of 10 %. A stem holder was attached to the load cell, which elevated the stem by 0.04 m above the bed. Pictures of

Table 1
Summary of the investigated material properties, including the surrogate materials used by Luhar and Nepf (2011) and the defined growth states based on field measurements of Keimer et al. (2023).

	Luhar and Nepf (2011)		Field data from Keimer et al. (2023)		
v (m/s)	0.04 – 0.32		0.50	0.50	0.50
Material	Soft foam	HDPE	Flowering	Broken	Sprouting
L_S (m)	0.05 - 0.25		0.20	0.20	0.20
W_S (m)	0.01	0.01	4.11×10^{-3}	3.97×10^{-3}	4.21×10^{-3}
T_S (m)	1.9×10^{-3}	0.40×10^{-3}	4.11×10^{-3}	3.97×10^{-3}	4.21×10^{-3}
ρ (kg/m^3)	670	950	670	670	670
E (kN/m^2)	500	930 000	323 460	225 270	133 780
Ca (–)	0.55 – 5500	0.032 – 320	0.53	0.85	1.20
B (–)	2.7 – 340	0.0049 – 0.62	0.057	0.088	0.13

the stem motion were captured for the shortest (0.05 m) and longest stems (0.25 m) in combination with a medium (0.16 m/s) and the highest (0.32 m/s) current velocity using a camera. The reference experiment used two different materials, HDPE and soft foam. The stiffer HDPE material was characterized by a Young's modulus of 0.93 GPa, a density of 950 kg/m^3, and a thickness of 0.0004 m. The more flexible soft foam material had a Young's modulus of 500 kPa, a density of 670 kg/m^3, and a thickness of 0.0019 m. The stems were 0.01 m wide. The material properties are summarized in Table 1, including the dimensionless Cauchy number (Ca) and Buoyancy parameter (B) as defined by Luhar and Nepf (2011). For more details of the experimental set-up, the reader is referred to Luhar and Nepf (2011).

The afterward applied vegetation properties from the field are additionally summarized in Table 1. To mimic the cylindrical live vegetation, the width and thickness of the modeled stem were chosen equal to the measured diameter. In the field, the height of the different growth states differed as well, leading to an average stem height of the flowering plant of 0.30 m, of the broken plant to 0.22 m and of the sprouting plant to 0.07 m. For the simulations of the application case, the stem heights have been selected to be equal, ensuring a focus on the comparison of the material properties like Young's modulus and the second moment of area instead of giving the main focus to the stem height. Potentially, the difference in the resulting flow conditions would be even larger. As Keimer et al. (2023) did not measure the plant density, the density of the soft foam material was applied to all growth states. As a further simplification, the damping coefficients have been set to $c_d = 1$ and $c_k = 5 \times 10^{-10}$ for all growth states. The dimensionless numbers are calculated similarly to Luhar and Nepf (2011), showing that the Cauchy numbers of all growth states lay within the range of tested Cauchy numbers from the reference experiment. Additionally, the Buoyancy parameters are in a comparable order of magnitude as the tested soft foam material, partly due to the selected same material density.

A numerical current flume has been set up to reproduce the reference experiment, a sketch is displayed in Fig. 2. For the side walls of the flume, wall functions with no-slip boundary conditions are used. As recommended by Tschisgale and Fröhlich (2020), a flume width of 0.16 m is chosen. The results's sensitivity in regard to flume width is analyzed in the framework of this study. For the inflow, a constant velocity profile is used, similar to the reference experiment. For both, in- and outflow boundary conditions, the water depth was kept constant at 0.30 m, with a fix level set to ensure numerical stability. For the validation with numerical results, the model set-up has been selected accordingly to Tschisgale and Fröhlich (2020) to ensure comparability. The cell size of the uniform grid is therefore equal to 0.5×10^{-3} m. The convergence study conducted in the Appendix A shows that the simulation converges for the applied cell size.

Following a grid convergence study in the Appendix A, various simulations have been run to investigate the research objectives posed in Section 1. The influence of the individual, rigid elements that the modeled stem consists of has been tested through a sensitivity analysis (see Appendix A) in order to find an independent solution and ensure accurate computability. The model performance is studied regarding its potential to accurately simulate the drag force and stem motion for varying stem lengths, material properties, and current velocities. Afterward, the influence and suitability of the turbulence model for the structural solver have been studied by comparing the performance of RANS, URANS, and LES. For the first two approaches, RANS and URANS, the k-ω model has been selected as it is widely applied by the developers of the employed numerical model – see for example Bihs et al. (2016), Sasikumar et al. (2020), and Martin and Bihs (2021). Finally, the time-dependent influence of the damping coefficients on the resulting forces and stem motion has been investigated and the capabilities of the model have been emphasized by applying field data from live vegetation to the proposed model.

The simulations were run on the Phoenix-Cluster of the TU Braunschweig, Germany, which provides 304 nodes in total, each equipped with dual CPU INTEL Xeon E5-2640v4@3.4 GHz and 64 GB RAM. The simulations were run on two nodes, resulting in 40 processor cores per simulation. The grid was generated with a mesh generator, DIVEMesh, and the simulations used REEF3D::CFD, both version v230614.

The results of the convergence study are summarized in Table A.3 in the appendix, and confirm the assumption that a fine grid close to the flexible stem is crucial for the resulting forces. The resulting non-uniform grid for the current simulations can be seen in Fig. 3. Note that the refined area around the stem in the x- and z-direction is adapted proportionally to the stem lengths to ensure comparable conditions for the different stems. Considering the available computational resources in the case of the longest stem, the refined length was set to $F = 1.2L_S$, while the refined length in y-direction was 0.04 m for all tested cases. With a stretching factor of 1.1, the cell size varied from 1.5×10^{-3} m in the refined area to 0.03 m in the coarser area. That setup results in ~ 1.1M cells for the 0.05 m stem and ~ 4.5M cells for the 0.25 m stem.

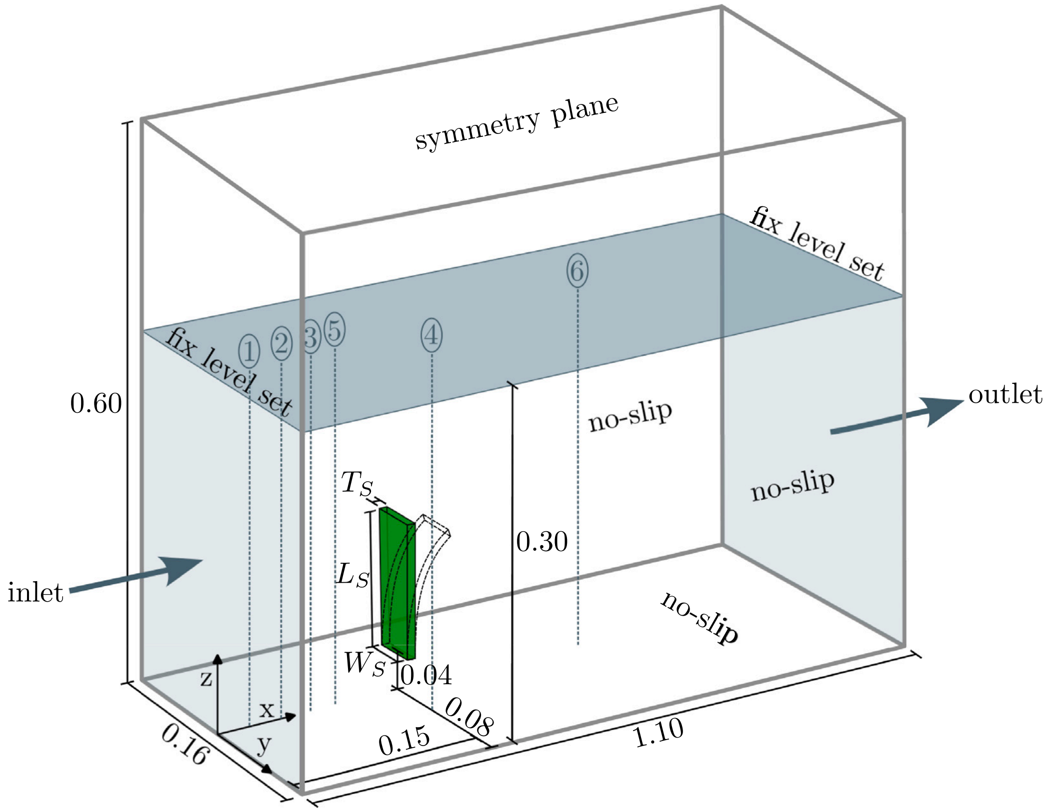

Fig. 2. Sketch of the numerical model set-up for the current simulations, including the thickness of the stem (T_S), the length of the stem (L_S), the width of the stem (W_S), and the positions of the applied line probes 1–6, dimensions in m (not to scale).

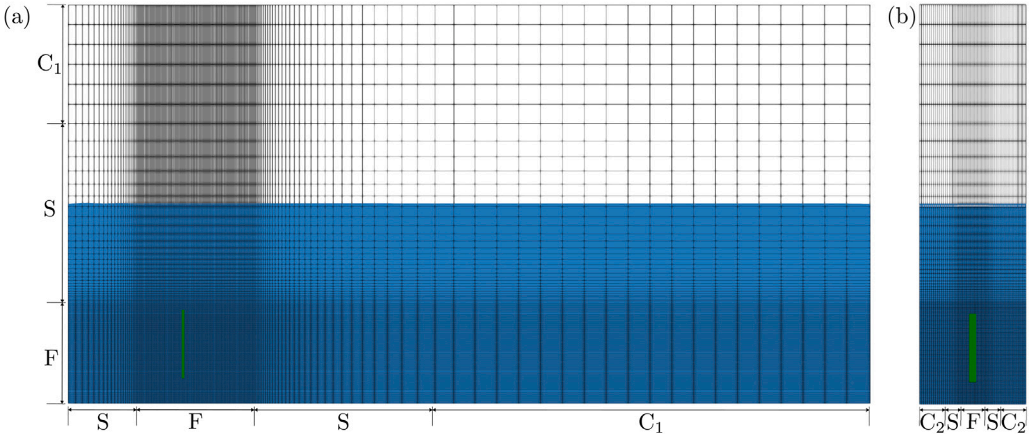

Fig. 3. Non-uniform grid in (a) side view and (b) front view, distances shown for the 0.1 m long stem. The fine grid (F) cell size is 1.5×10^{-3} m, followed by a stretching zone (S) with a factor of 1.1, and a coarse grid (C_1 = 0.03 m and C_2 = 3.0×10^{-3} m).

3. Results

3.1. Velocity field and influence of turbulence modeling

Before a detailed investigation of the complex FSI, it is paramount to test and select a model family on the fluid part that governs the process of eddy production and detachment in the vicinity of the dynamic stem motion. In terms of model families, RANS, URANS, and LES fluid solvers have been tested with a variety of parameter settings; the accuracy that could be obtained

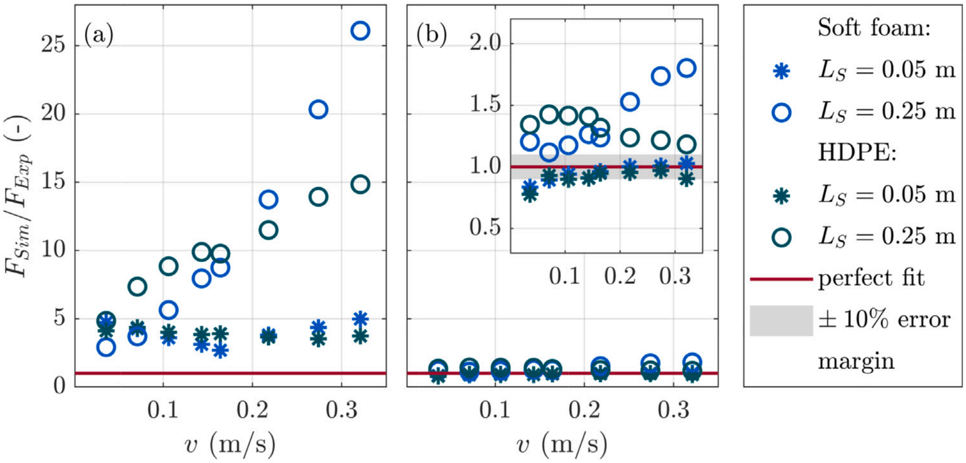

Fig. 4. Comparison of simulated vs. experimentally-derived forces (Luhar and Nepf, 2011), for both the soft foam and HDPE Material and two stem lengths $L_S = 0.05\,\mathrm{m}$ and $L_S = 0.25\,\mathrm{m}$ with (a) RANS and (b) wall-adapted RANS turbulence modeling; inset shows the same data but with adjusted y-axis scale.

by the FSI has then been compared to an experimental dataset (Luhar and Nepf, 2011), and against results of a recently published numerical study (Tschisgale and Fröhlich, 2020).

First, the influence of the wall-adapted RANS approach on the FSI is presented and compared to the RANS approach without modification. The resulting forces for a variation of tested material types, stem lengths, and current velocities are compared between RANS and the wall-adapted RANS approach in Fig. 4. The resulting stem bending between the two approaches is compared for a selected test case in Fig. 5. It can be observed that the RANS simulations, using the k-ω turbulence model without wall-adaption, overestimate the forces measured in the reference experiment. While the overestimation of the forces for the 0.05 m long stem remains the same order of magnitude independent of the current velocity, the overestimation by the numerical model increases for the 0.25 m long stem with higher current velocities (Fig. 4a). In contrast, the resulting forces with the wall-adapted RANS approach are in the same order of magnitude as the experimental results, see Fig. 4b. Nevertheless, the forces for the 0.25 m long stem are overestimated by 20 % to 40 % for the HDPE material and by 10 % to 80 % for the soft foam material.

The large observed deviations between the resulting forces for the RANS compared to the wall-adapted RANS approach render an evaluation of the occurring processes essential. Fig. 5 compares the resulting flow field around the stem for the 0.25 m long HDPE stem with a current velocity of 0.16 m/s for the RANS and the wall-adapted RANS approach, providing further insights and possible explanations for occurring differences. It can be seen that the simulation using the RANS turbulence model also overestimates the bending position compared to the resulting bending of the wall-adapted RANS approach, even though the incoming flow field does not vary. The overestimation of the bending and forces in the RANS simulations without wall-adaption is likely due to the turbulent kinetic energy generated near the stem being dispersed across a broader area within the flow field by the RANS turbulence model, which appears to inhibit the recirculation of the flow field beneath the stem, resulting in its excessive bending. This effect can be prevented by enhancing the turbulent energy dissipation in the proximity of the stem, as introduced in Section 2, utilizing the wall-adapted RANS approach. The resulting stem bending and surrounding flow field of the wall-adapted RANS approach provide a more reasonable FSI, depicted in Fig. 5b. In conclusion, the wall-adapted RANS is considered more suitable for simulating the FSI within the FD CFD model compared to the non-adapted RANS approach. Consequently, the wall-adapted approach is employed for further comparison with results from other turbulence models, including URANS and LES.

Fig. 6 compares the simulated results for the wall-adapted RANS, URANS, and LES simulations for both the HDPE and soft foam material. Independent of the selected turbulence model and the tested material type, the resulting forces of the 0.05 m stem are in high agreement with the experimental forces, with the majority being within the estimated error margin of ±10 % of the experimental force sensor. In contrast, the forces of the 0.25 m long stem are generally overestimated. In Fig. 6b the numerical results using URANS with the k-ω turbulence model have the tendency of being higher compared to those obtained with the wall-adapted RANS turbulence model (Fig. 6a). The force computed for the 0.25 m long stem overestimates the experimental results by a factor of 1.5 for the HDPE material and over 2 for the fastest current velocity for the case of the soft foam material. Smaller deviations to the experimental data could be observed using LES in Fig. 6c. Especially for the 0.05 m long stem, the deviations of the simulated to the experimental forces are for seven out of eight investigated velocities within a ± 10 % error margin. Larger deviations can be seen for the 0.25 m long stem, pointing out that accurate modeling of the turbulence is especially crucial with longer stem lengths.

Concluding the comparison between the resulting FSI for different turbulence models, Fig. 7 depicts the flow fields and resulting bending positions of the stem for the wall-adapted RANS, URANS, and LES. It becomes apparent that utilizing the wall-adapted RANS and URANS results in a similar flow field and stem bending position (Fig. 7a and Fig. 7b). As anticipated, the LES results differ in the flow field due to its ability to resolve larger eddies (Fig. 7c). Nevertheless, the stem bending results are in the same position for all herein compared to the turbulence models.

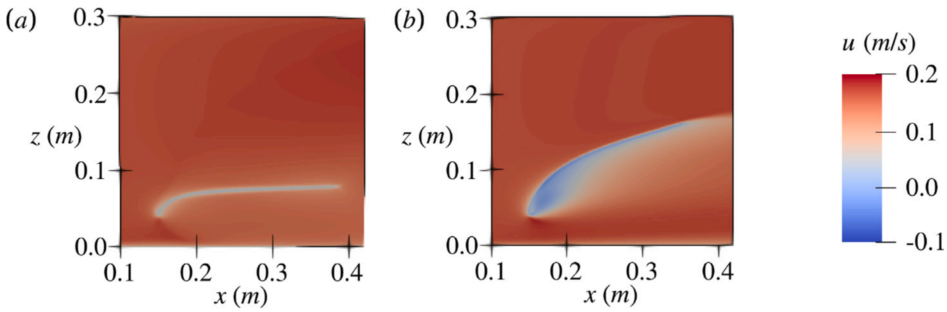

Fig. 5. Simulated flow field for the 0.25 m long stem with HDPE Material and a current velocity of $0.16\,\mathrm{m/s}$, comparing the simulations results of (a) RANS and (b) wall-adapted RANS approach.

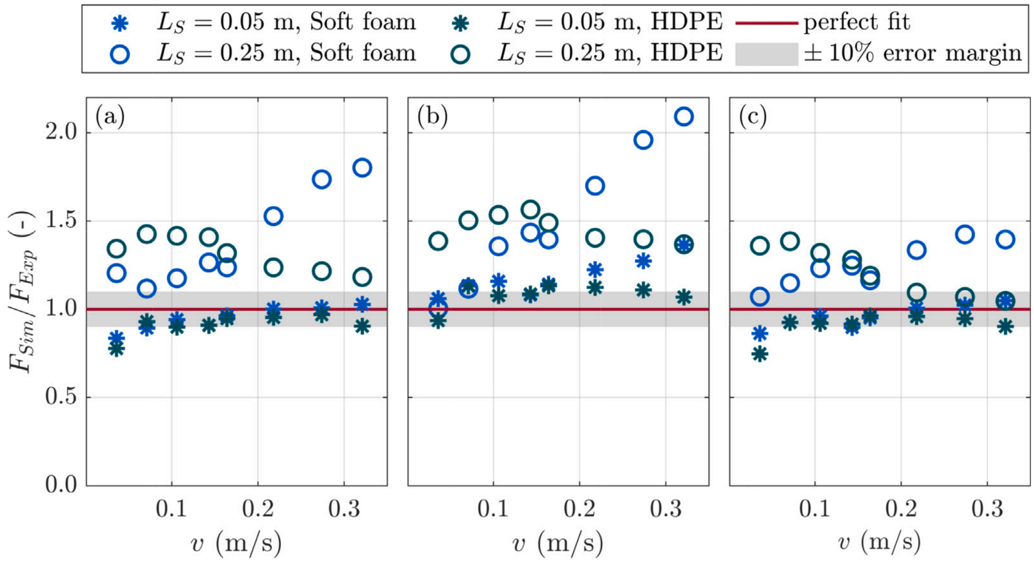

Fig. 6. Comparison of simulated vs. experimentally-derived forces (Luhar and Nepf, 2011), for both the soft foam and HDPE Material and two stem lengths $L_S = 0.05\,\mathrm{m}$ and $L_S = 0.25\,\mathrm{m}$ with (a) wall-adapted RANS, (b) URANS and (c) LES turbulence modeling.

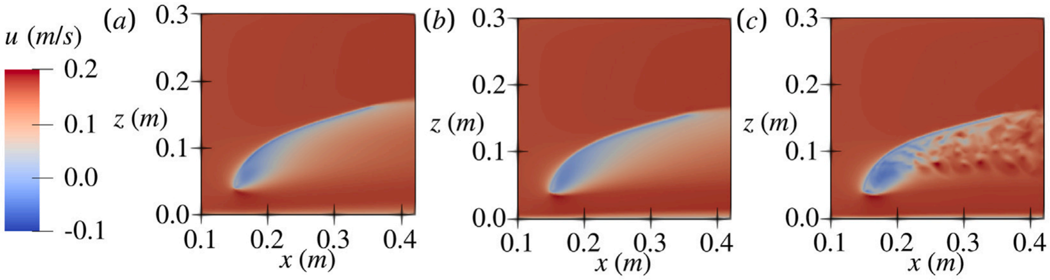

Fig. 7. Simulated flow field for the 0.25 m long stem with HDPE Material and a current velocity of $0.16\,\mathrm{m/s}$ comparing (a) wall-adapted RANS, (b) URANS and (c) LES turbulence modeling.

In summary, the wall-adapted RANS approach enhances the FSI in the FD CFD solver, confirmed by the resulting reasonable forces and stem bending. Similar stem bending can be observed when comparing different turbulence model families, including wall-adapted RANS, URANS, and LES. However, LES demonstrated the closest alignment with experimental results in terms of force deviations, making it the preferred turbulence modeling approach for this study.

As the resulting forces are sensitive to the chosen turbulence model, the sensitivity regarding the SGS model and their corresponding coefficients was also tested. Fig. 8a visualizes the resulting force deviations for the WALE and Fig. 8b for the Smagorinsky SGS model. The constant C_W applied in the WALE model has been varied between 0.30 and 0.60, and the Smagorinsky

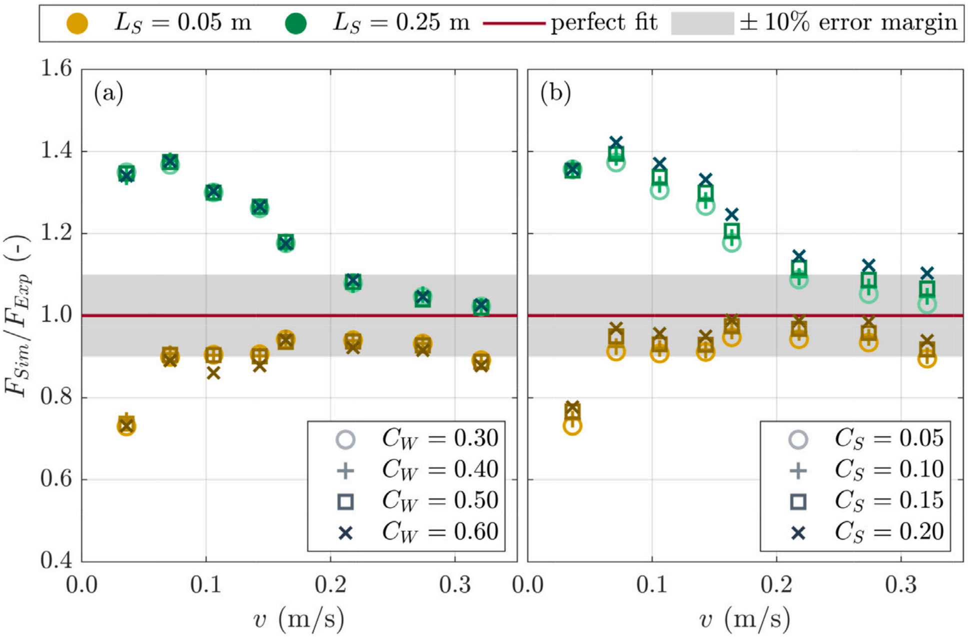

Fig. 8. Simulated forces in relation to experimental forces (Luhar and Nepf, 2011) for both the HDPE Material and two stem lengths $L_S = 0.05$ m and $L_S = 0.25$ m with (a) using the WALE SGS-model and a variation of WALE-coefficients and (b) Smagorinsky SGS-model and variation of Smagorinsky coefficients.

constant C_S has been varied between 0.05 and 0.20, covering a wide range, to enable a general comparison of its influence. Fig. 8a shows that the variation of C_W has, for most simulations, no influence on the resulting forces. Correspondingly, the mean difference between the resulting forces for the smallest and largest C_W is 1.87 % for $L_S = 0.05$ m and 0.52 % for a stem length of 0.25 m. On average, using a C_W of 0.40 leads to an underestimation of 10.50 % for the 0.05 m long stem and to an overestimation of 20.09 % for the 0.25 m long stem. By contrast, it can be observed in Fig. 8b that, with larger C_S, the resulting numerical forces increase and thus the deviation from the experimental results increases. The comparably larger influence of the chosen C_S is outlined by the mean difference between the resulting forces of the smallest and largest C_S, being 4.70 % for $L_S = 0.05$ m and 3.31 % for $L_S = 0.25$ m. The deviations to the experimental forces using a C_S of 0.10 are in a similar range to $C_W = 0.40$, resulting in an underestimation of 9.00 % for the 0.05 m long stem and an overestimation of the 0.25 m long stem by 21.84 %.

The value of C_S has been chosen equally to 0.10, as it leads to less overestimation of the simulated forces for the 0.25 m long stem compared to the results using $C_S = 0.15$ and 0.25 and less underestimation of the simulated forces for the 0.05 m long stem compared to the results with $C_S = 0.05$. Additionally, the recommended range of values for C_S, depending on the source, lies between 0.10 and 0.20. Ferziger and Perić (2002), Katopodes (2019) and previous studies using the same numerical model (Cui et al., 2022a,b) have successfully applied a C_S value of 0.10 for their LES studies.

Further validation of the accuracy of the numerical simulation of the FSI was achieved using published numerical results by Tschisgale and Fröhlich (2020). Their spatial velocity information of the FSI was compared to the results of the FD CFD solver in the x-direction (u), as shown in Fig. 9, for an inflow velocity (v) of 0.16 m/s. Overall, the qualitative comparison of the flow fields in Fig. 9 leads to the conclusion that the results of the simulation are comparable to the output of the solver used by Tschisgale and Fröhlich (2020). The minimum and maximum velocities are in a comparable order of magnitude for the selected time step, ranging from −0.60 m/s to 1.47 m/s for the results of Tschisgale and Fröhlich (2020) and from −0.56 m/s to 1.33 m/s for the results of this study. Overall, the turbulence of the wake distributes over a similar area behind the stem for both simulated flow fields. At the base of the stem, the wake extends over a larger area and small eddies are less visible in the FD CFD solver compared to the results of Tschisgale and Fröhlich (2020). The latter is likely due to the use of different spatial discretization methods. Tschisgale and Fröhlich (2020) used a second-order central differences method, while the FD CFD solver in this study was developed for the fifth-order weighted essentially nonoscillatory (WENO) method, which is known to be more diffusive but provides more stability (Xu and Shu, 2005; Bihs et al., 2016).

The tip position of the two simulations deviates by 4 % of the stem length. While the simulated tip position of Tschisgale and Fröhlich (2020) shows good agreement with the reference experiment with a deviation of 2 % relative to the stem length, this study shows a slightly better agreement with a relative deviation of the tip position of 1.8 % compared to the experimental tip position. The resulting forces are in the same order of magnitude ($F_{sim} = 0.0074$ N and $F_{simT} = 0.0076$ N) and in agreement with the measured experimental force ($F_{exp} = 0.0077$ N).

Fig. 10 additionally compares the normalized horizontal velocity for four different locations behind the stem for one time step. Overall, it can be seen that the influence of the stem on the flow is in similar areas in z-direction for all locations. The deviation of

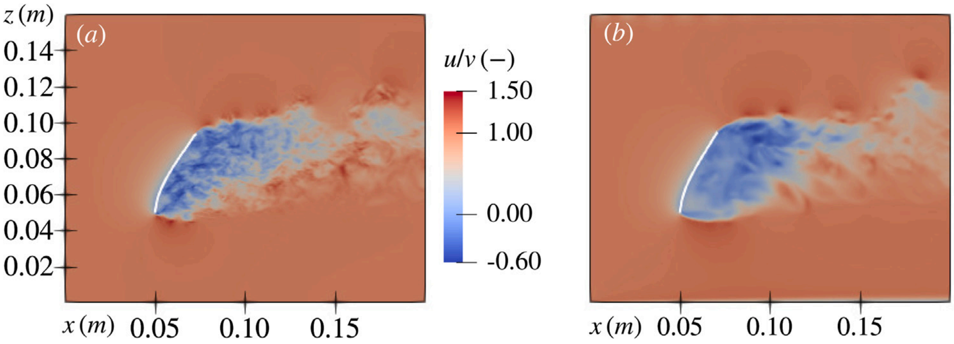

Fig. 9. Comparison of the normalized horizontal velocity (u/v) with L_s = 0.05 m, v = 0.16 m/s and the soft foam material with (a) the simulated results of Tschisgale and Fröhlich (2020) and (b) the simulated results of this study.

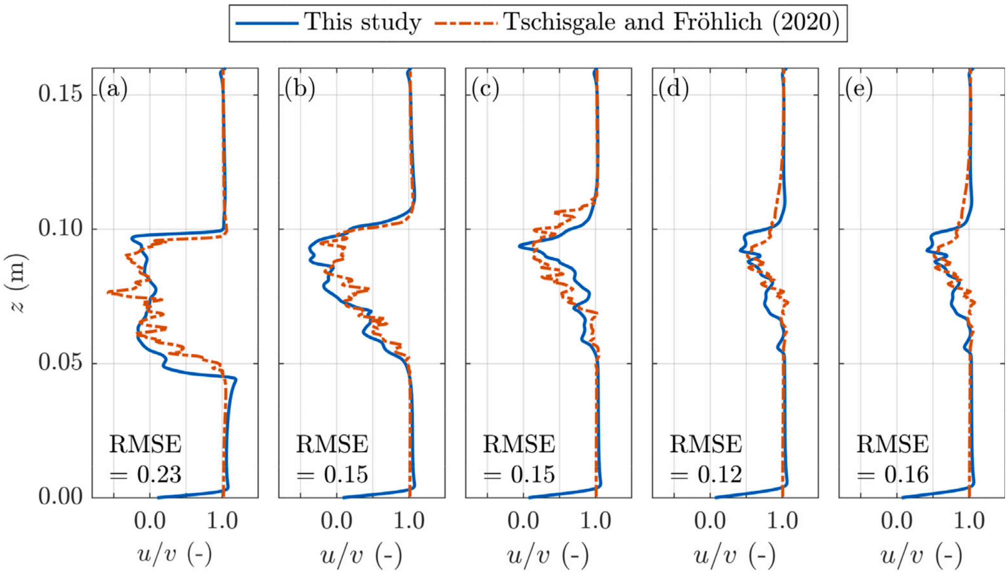

Fig. 10. Comparison of the normalized horizontal velocity over the flume height for this study and the results of Tschisgale and Fröhlich (2020) at different positions behind the stem with y = 0.00 m and x = (a) 0.075 m, (b) 0.10 m, (c) 0.125 m, (d) 0.15 m and (e) 0.175 m.

the normalized horizontal velocity is largest close to the stem (Fig. 10a) with the RMSE equal to 0.23 and in a similar magnitude for the other locations (RMSE = 0.12 - 0.16). The minimum and maximum normalized velocities are in the same range for both simulations, even though the negative peak is slightly higher for the simulations of this study in locations b to e. Additionally, the before observed enhanced diffusivity of the FD CFD solver can be seen as well due to the larger fluctuations of the horizontal velocity over the flume height for the simulations of Tschisgale and Fröhlich (2020).

A thorough calibration and validation approach has provided confidence that the chosen LES approach is resulting in good agreement of simulated drag forces, bending motion and the resulting velocity profile of flexible vegetation in the FD CFD solver compared to both results of physical experiments and numerical simulations. In the next sections, further parameters, such as the fluctuations of the stem in the current-induced flow and the resulting turbulence intensity are evaluated.

3.2. Variation of material properties and hydrodynamic conditions

Within this section, the simulated results for several stem lengths, current velocities, and material properties are presented. The comparison of the simulated forces to the forces measured in the reference experiments for all tested stem lengths and current velocities for the HDPE material is shown in Fig. 11. It can be observed that independent of stem length and current velocities, most simulated forces are within a range of ± 10 % around the measured forces of the reference experiment. A single case (0.05 m stem in combination with the lowest current velocity) showed a slightly higher deviation, underestimating the experimental force by more than 10 %. In contrast, the experimental forces are overestimated for the 0.25 m stem with current velocities lower than 0.16 m/s. In general, it appears that the deviation between the simulated and experimental forces is larger for lower current velocities. In

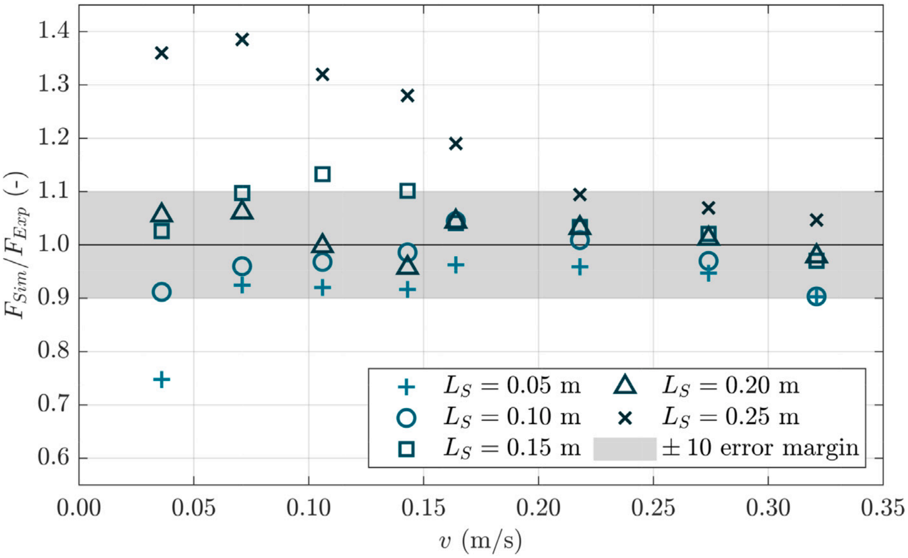

Fig. 11. Resulting normalized forces of the HDPE material for all current velocities and stem lengths.

contrast, the absolute error ($|F_{Exp} - F_{Sim}|$) is highest for the faster current velocity, with up to 0.0049 N compared to a maximum of 0.000 61 N for the lowest current velocity. This can be explained, as the overall magnitudes decrease, and even minor absolute errors resulting from inaccurate process representation become accentuated.

While drag forces are one important indicator proxy for the accuracy of a numerical model, it remains important to note that the deflection of the stem is a second important measure to judge the performance of the model. In addition, an analysis of the deflection may help to better interpret why an overestimated force for the lower current velocities for the HDPE material and the higher current velocities for the soft foam material (see Fig. 6c) occurs. Hence, the bending behavior of the two simulated materials is compared next (see Figs. 12 and 13). It should be noted that different positions of the longer stems have been observed throughout the reference experiments, as the flexible stems generally do not take a steady-state position while interacting with the flow field, and the turbulent motion of the flow leads to continuous stem movement. Luhar and Nepf (2011) selected therefore individual snapshots showing the observed variation in the stem position of the reference experiment, displayed in Fig. 12 and Fig. 13. The same can be observed in the numerical simulations, which is visualized as the gray area next to the average stem position for each simulation in Fig. 12 and Fig. 13. The gray area spans over the maximum and minimum positions of the stem. For the longer stems, it can be observed that the fluctuation is larger for both materials with faster current velocity. In addition, the fluctuations are higher for the more flexible soft foam material.

The relation between the tip deviation and the stem length is stated (Δ_{tip}/L_S) and displayed in Fig. 14. As for the forces, the bending of the smaller stem ($L_S = 0.05$ m) provides better agreement for both materials and velocities, with less than 3 % deviation in relation to the stem length. For the longer stem ($L_S = 0.25$ m), the bending provides good agreement for $v = 0.32$ m/s for the soft foam material (Fig. 12d) and for $v = 0.16$ m/s for the HDPE material (Fig. 13b) with 2.76 and 4.32 % deviation to the stem length, respectively. The bending of the simulated 0.25 m soft foam stem for the current velocity with 0.16 m/s is larger compared to that measured in reference experiment (Fig. 12b), with 9.44 % deviation in relation to the stem length. The same can be observed for the HDPE material with the faster current velocity (0.32 m/s, Fig. 13d), resulting in 9.52 % deviation in relation to the stem length. While having some variation within the simulated and experimental stem position, all resulting deviations in relation to the stem length are smaller than 10 % (see Fig. 14).

Together with the observations regarding the deviations of the simulated forces, the analysis of the deflection leads to the conclusion that the forces exerted onto the long stem are overestimated when the long stem is in the same spatial position as the stem in the experiment. The simulated forces are in accordance with the results of the reference experiment for the 0.25 m stem when the bending is larger than expected, for both types of material. Since the results of the stem bending have been only published for the 0.05 m, and 0.25 m long stems, it cannot be assessed if the deviation also occurs for the other stem lengths (0.10 m to 0.20 m).

3.3. Influence of the damping coefficients

The structural solver in the FD CFD solver necessitates the use of damping coefficients to take the non-linear viscous damping of rods into account, see also Eqs. (11) and (12). While this part of the FSI simulation seems straightforward, it has never been subject to an in-depth investigation, as to how these parameters influence the structural motion and, as a consequence, how it would then feed back into the flow field downstream of the FSI. This is, however, a rather important factor for follow-up studies, e.g., on sediment transport problems of soil around coastal vegetation.

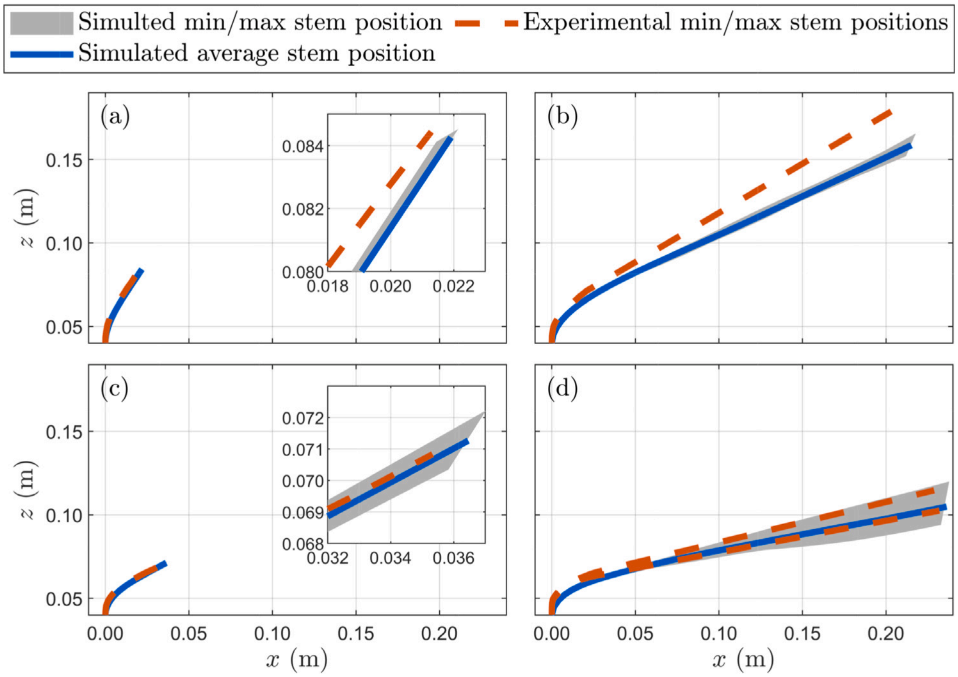

Fig. 12. Bending of the simulated and experimental stem (Luhar and Nepf, 2011) for the soft foam material with (a) L_S = 0.05 m and v = 0.16 m/s, (b) L_S = 0.25 m and v = 0.16 m/s (c) L_S = 0.05 m and v = 0.32 m/s and (d) L_S = 0.25 m and v = 0.32 m/s.

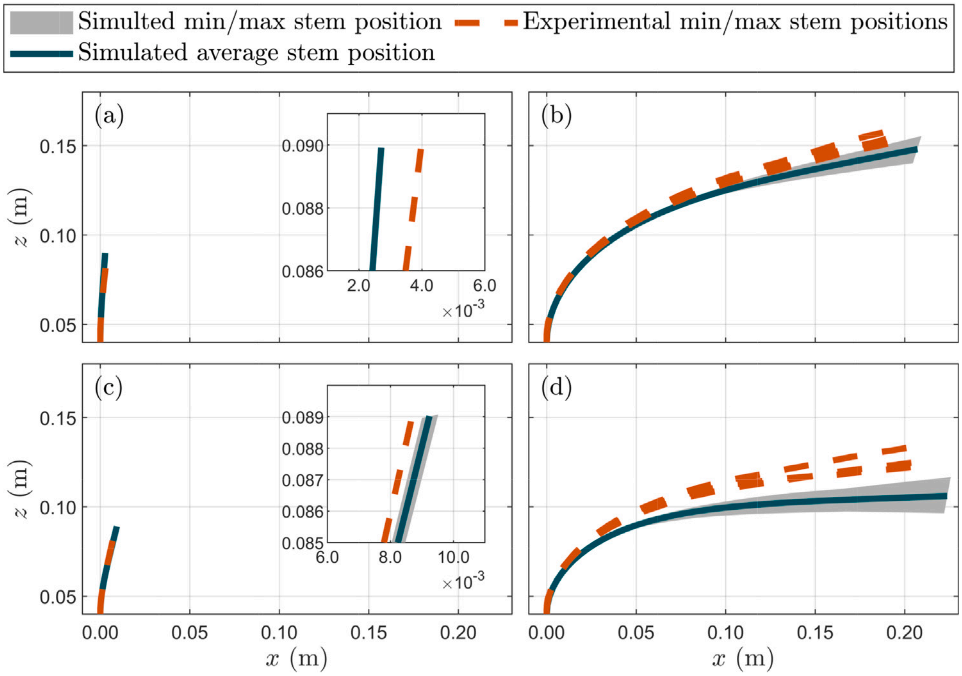

Fig. 13. Bending of the simulated and experimental stem (Luhar and Nepf, 2011) for the HDPE material with (a) L_S = 0.05 m and v = 0.16 m/s, (b) L_S = 0.25 m and v = 0.16 m/s (c) L_S = 0.05 m and v = 0.32 m/s and (d) L_S = 0.25 m and v = 0.32 m/s.

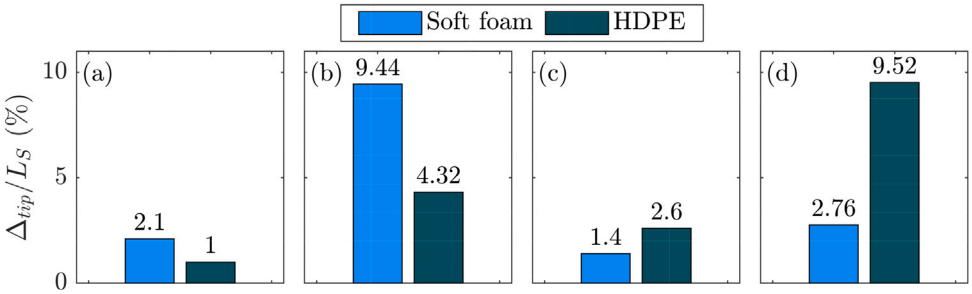

Fig. 14. Comparison of the tip position for the soft foam and the HDPE material with (a) $L_S = 0.05\,\mathrm{m}$ and $v = 0.16\,\mathrm{m/s}$, (b) $L_S = 0.25\,\mathrm{m}$ and $v = 0.16\,\mathrm{m/s}$ (c) $L_S = 0.05\,\mathrm{m}$ and $v = 0.32\,\mathrm{m/s}$ and (d) $L_S = 0.25\,\mathrm{m}$ and $v = 0.32\,\mathrm{m/s}$.

For the shorter and more rigid stems, the damping coefficients only influence the time between the initial position and the steady-state bending, as their movement is minimal. In contrast, Fig. 12b and d as well as Fig. 13b and d show that the 0.25 m-stem continuously undergoes a movement with a magnitude of centimeters in z-direction, most visible for the 0.25 m long soft foam stem with the fastest current velocity ($v = 0.32\,\mathrm{m/s}$) with a movement of 0.03 m in z-direction.

To investigate the potential influence of the damping coefficients on the dynamic stem movement of the longest soft foam stem, the setup with a current velocity of 0.32 m/s is tested for a variation of the damping coefficients. Hereby, only c_k is varied, as c_d was examined to not influence the bending behavior of the stem and is therefore kept constant ($c_d = 1$). It should be noted that the damping coefficients only have a minor influence on the average forces (e.g. $c_k = 1 \times 10^{-4}$, $F_{sim} = 0.023\,\mathrm{N}$, for $c_k = 1 \times 10^{-5}$, $F_{sim} = 0.022\,\mathrm{N}$ and for $c_k = 1 \times 10^{-7}$, $F_{sim} = 0.021\,\mathrm{N}$).

The time history of the drag force, representative of the influence of the damping coefficient on the stem movement, is plotted in Fig. 15a-c. A low-pass filter and a Tukey window have been applied to the simulated drag forces to reduce the effect of leakage for the fast Fourier transform (FFT). A filter width of 150 Hz has been selected for the low-pass filter, ensuring that only the smallest fluctuations are filtered without discarding effects in the range of 0 Hz to 1 Hz, which has been shown relevant in the further analysis. To provide a broader comparison, the natural frequency of the blade has been calculated with the constant $C_n = 0.56$ and the assumption of C_M being equal to 1 (Luhar and Nepf, 2016):

$$f_n = C_n \sqrt{\frac{EI}{L_S^4(\rho_S W_S T_S + \rho C_M(\pi T_S^2/4))}} \tag{14}$$

The force amplitude spectrum for the three cases with varied damping coefficients in the frequency domain are compared in Fig. 15d. The highest damping coefficient shown here ($c_k = 1 \times 10^{-4}$) appears to dampen the larger force fluctuations that occur for the two other damping coefficients, which is also apparent due to the peak at a much smaller frequency (0.01 Hz) compared to the other two peaks (0.20 and 0.22 Hz). The results for the other two damping coefficients are similar, suggesting that a threshold value appears from which the force variation is limited. The reduced variation of the resulting forces can suggest a restricted movement of the flexible structure.

To evaluate the influence of variation of damping coefficients applied to the stems on the flow field, the turbulence intensity TI has been calculated using the time-averaged velocity $\bar{u}$ and u_{rms}:

$$TI = \frac{u_{rms}}{\bar{u}} \text{ with } u_{rms} = \sqrt{\overline{(u(t) - \bar{u})^2}} \tag{15}$$

Here, the TI is used as an indicator of the impact of the stem to the flow field for two locations, one in front of the stem ($x = 0.10\,\mathrm{m}$, $y = 0.00\,\mathrm{m}$), representing the undisturbed flow field and a second one in the wake of the stem ($x = 0.40\,\mathrm{m}$, $y = 0.00\,\mathrm{m}$), depicted in Fig. 2 as line probe 5 and 6. Fig. 16 displays the resulting normalized mean horizontal velocity, the RMS of the time track of the horizontal velocity, and the resulting TI for both locations. The results show that the stem influences the flow field behind by reducing the horizontal velocity (Fig. 16a). The extent of reduction differs depending on the applied damping coefficient. The fluctuations of the horizontal velocity, expressed by its RMS, have a varying extent for different damping coefficients (Fig. 16b), whereby the results for $c_k = 1 \times 10^{-7}$ differ the most. The resulting TI has similar trends (Fig. 16c), showing that the use of a smaller damping coefficient leads to less turbulence in the flow field for the selected position. While the turbulence conditions in front of the blade can be classified as low turbulence (< 1 %), the results with $c_k = 1 \times 10^{-7}$ fall into the category of mid turbulence and with $c_k = 1 \times 10^{-4}$ and $c_k = 1 \times 10^{-5}$ as high turbulence with $TI > 10\,\%$ (Windt et al., 2021).

3.4. Application of field data

Providing further insights of the capability of the proposed model, different vegetation parameters from field measurements, see Table 1, are applied to the numerical model and its outcomes compared. For the same horizontal current velocity of 0.50 m/s, the resulting drag force, bending angle, and drag coefficient are provided in Table 2. The applied bending angle follows the definition of Luhar and Nepf (2011) and is accordingly given relative to the initial stem position. The angle is determined at mid of the stem

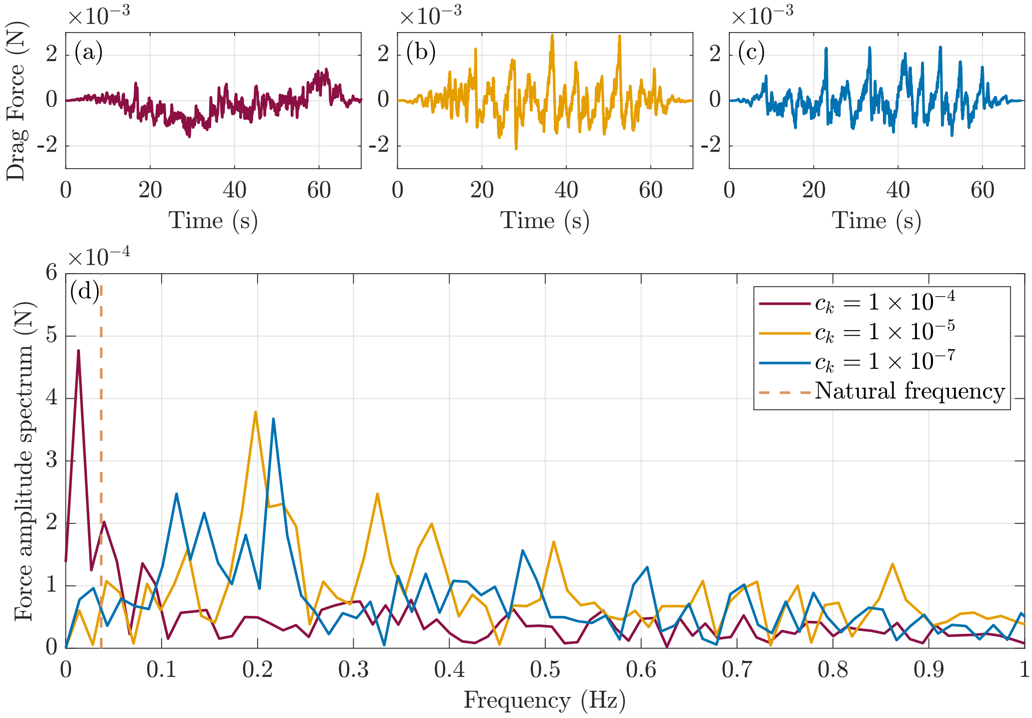

Fig. 15. Filtered simulated drag force for varying damping coefficients in the (a-c) time histories and (d) force amplitude spectra, including the natural frequency of the stem.

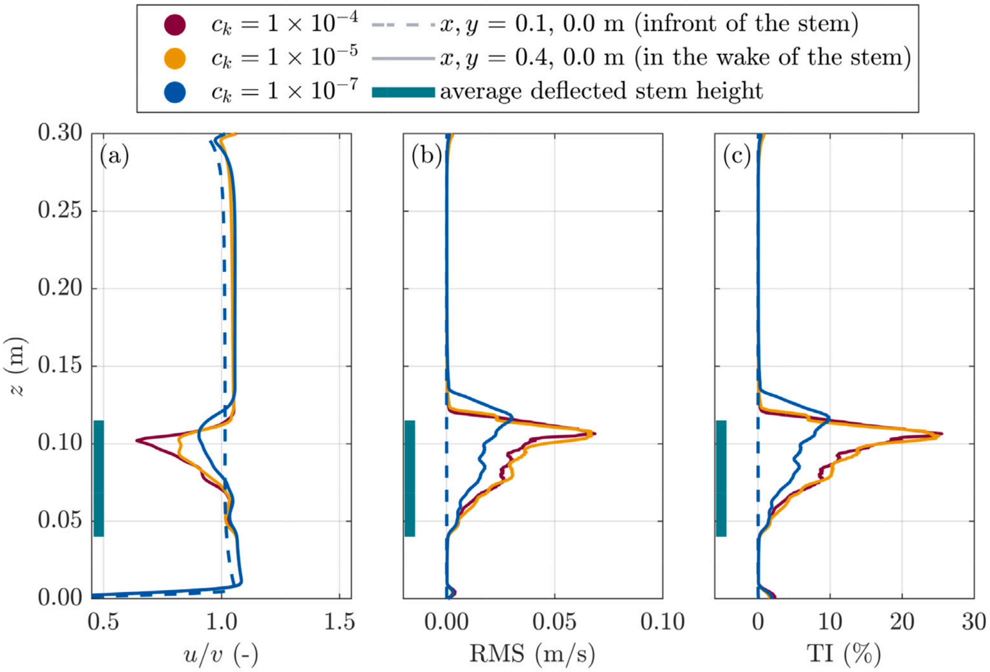

Fig. 16. (a) Normalized horizontal flow velocity, (b) RMS of the horizontal velocity, and (c) resulting turbulence intensity compared for three different damping coefficients in front of (probe line 5) and behind (probe line 6) the stem. The results for probe line 5 are identical, independent of the applied damping coefficient.

Table 2
Resulting parameters from simulations with different growth states and a current velocity of 0.50 m/s.

Growth state		Flowering	Broken	Sprouting
Drag Force	F_D (N)	0.19	0.18	0.18
Bending angle	ϕ (°)	8.65	13.32	18.18
Drag coefficient	C_D (-)	0.73	0.67	0.58

and calculated by $\phi = 90° - tan^{-1}((z_{tip} - z_{mid})/(x_{tip} - x_{mid}))180/\pi$, with z_{tip} and x_{tip} describing the bent position at the tip of the stem and z_{mid} and x_{mid} the bent stem position at half of the stem length. The drag coefficient was calculated with the equation from Luhar and Nepf (2011), resulting in $C_D = F_D/(0.5\rho W_S v^2 cos(\phi)^2)$.

The results show that the same plant species in different growth states have comparable drag forces (0.19, 0.18, and 0.18 N) while differing in their resulting stem bending, here expressed by bending angles (8.65°, 13.32°, and 18.18°). Consequently, the calculated drag coefficients differ, even though their average forces are of similar magnitude, with the flowering plant having the highest drag coefficient (0.73), followed by the broken plant (0.67) and the sprouting state (0.58). The variation of resulting drag coefficients emphasizes the need for advanced numerical models that do not require the use of drag coefficients to be able to simulate live vegetation, as long as drag coefficients for individual plant species including seasonality are not available.

Further on, the results are compared and confirmed by an approach based on non-dimensional parameters and empirical relations. Luhar and Nepf (2011) proposed to use the effective length l_e to calculate the drag force ($F_D = 0.5\rho C_D b l_e U^2$). The effective length is determined by an empirical relation between Ca and B:

$$\frac{l_e}{l} = 1 - \frac{1 - 0.9Ca^{-1/3}}{1 + Ca^{-3/2}(8 + B^{3/2})} \tag{16}$$

The calculated effective length for the flowering stem is 0.20 m, for the broken stem 0.19 m, and for the sprouting stem 0.18 m. When using a C_D of 1.95 (following Luhar and Nepf (2011)), the calculated drag force is 0.20 N for the flowering stem and 0.18 N for both the broken and sprouting stem, which are in high agreement with the simulated forces (cf. Table 2). The high agreement underlines both the capability of the proposed model to simulate the resulting forces and the empirical model of Luhar and Nepf (2011) to determine the resulting forces based on the dimensionless parameters Ca and B.

Overall, relatively stiff vegetation has been chosen for this application study, underlined by the calculated effective length being almost equal to the initial stem length, resulting in a limited influence of the stem reconfiguration on the resulting forces. Future investigations should include more flexible live vegetation to confirm the general applicability of that approach and the proposed model.

Providing further insights into the resulting flow field behind the stems, the stem position, the normalized horizontal velocity, and the turbulence intensity for the three growth states are illustrated in Fig. 17c. This analysis follows the methodology previously described for the variation of damping coefficients presented in Section 3.3. The normalized horizontal flow velocity varies with height across different growth states (Fig. 17b), induced by the varying positions of the bent stems (Fig. 17a). The resulting turbulence intensity for each growth state is depicted in Fig. 17c. While the comparison reveals similar maximum values of the turbulence intensity at around 25 % for all growth states, large differences regarding their profile in z-direction become apparent.

The comparison indicates that the turbulence dynamics in the wake of the stem vary depending on the growth state, which can, for example, become relevant when looking at the sediment transport behavior in the proximity of the stem.

4. Discussion

4.1. Applicability of the model

The importance of choosing a suitable turbulence model to accurately simulate the flexible stem motion and the corresponding forces of the FSI has been highlighted in Section 3.1. The approach of a wall-adapted RANS turbulence model to improve the FSI shows promising results compared to the RANS approach without adaption. Its application should be the subject of future investigations, such as evaluating the influence when varying the incorporated turbulence factor, which enhances the turbulent energy dissipation. Based on that, the wall-adapted RANS approach can be a viable option for test setups including FSI when LES is not the favorable turbulence model. However, Fig. 6 shows that the resulting forces are in the highest agreement with the experimental results when utilizing the LES turbulence model. As a potential explanation, the resolved eddies close to the surface of the structure could be crucial to simulate the motion and forces correctly, and they can be simulated using the LES approach. A variation of the Smagorinsky coefficient C_S has been studied, revealing that lower values of C_S result in smaller forces applied on the stem. In contrast, Tschisgale et al. (2021) varied C_S (0.075, 0.15, 0.30) and observed no differences in the resulting mean velocity and the resolved turbulent shear stress of a flexible vegetation meadow. Those differing findings imply that parameter choices regarding the SGS model are not relevant when looking at the flow field of a vegetation meadow but certainly for the coupled forces of individual stems.

Previous studies (Tian et al., 2014; Tschisgale and Fröhlich, 2020), focused on simulating a rather short stem (i.e., 0.05 m), replicating the reference experiments. The FSI for such a short stem is dominated by compression flow and the stem only responds with minimal deflection (cf. Fig. 18), which is well represented by the structural solver used in this study. Moreover, it also produces accurate results for the longer stem lengths, especially stem lengths up to 0.20 m, see Fig. 11. In general, the numerical model shows

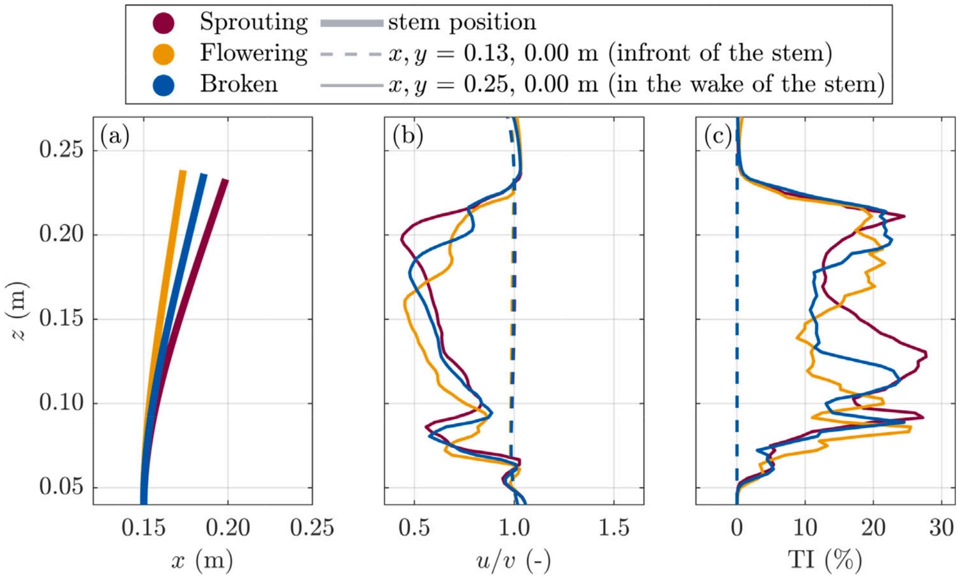

Fig. 17. (a) Stem position in steady state, (b) normalized horizontal flow velocity, and (c) resulting turbulence intensity, compared for three different growing states in front of and behind the stem.

consistent results independent of the stem length regarding the relationship between stem curvature and resulting drag forces. To evaluate that relationship, the deflected stem height (H_{df}) has been defined in this study as the highest point (in the z-direction) the stem reaches on average in its bent position. In Fig. 18, H_{df} is displayed with the simulated forces for the HDPE material. While H_{df} has a deviation of less than 2 % to L_S for the shorter stems for all current velocities ($H_{df} \approx L_S$), it differs highly for the longer stems ($H_{df} < L_S$). The latter case has been highlighted in Fig. 18 and a fitted curve was added. As expected, smaller H_{df} correlate with higher simulated forces independent of the initial stem length. Fig. 18 shows that the FSI in this study is consistent in simulating forces respective to the resulting deflected stem heights H_{df} for all simulated current velocities and stem lengths.

In Section 3.3, the importance of studying the damping coefficients for the flexible stem motion has been shown. The accurate simulation of the stem motion under currents has potential implications for future studies. In particular, when investigating the flow through a vegetation patch is considered in combination with sediment transport. There, the feedback of the vegetation-influenced flow field is crucial to the sediment mobility solution, see Le Bouteiller and Venditti (2015), Huai et al. (2019), Lou et al. (2021), Liu et al. (2022). The difference of the time-dependent variation for selected damping coefficients could not be validated through the reference experiments in this study, since transient behavior is often not recorded or published for current investigations. Therefore, to gain an improved understanding, time-dependent measurements of the forces for current experiments are required to enable a comparison of the resulting stem motion in the frequency domain. Even though the damping coefficients do not influence the average forces under currents, suitable damping coefficients are required to simulate the resulting forces for stem motion under waves (Martin and Bihs, 2021). As the damping coefficients are specific for the geometrically exact Cosserat rod, damping coefficients for other beam theories from the literature are challenging to apply, and their material dependency requires further investigation.

4.2. Model limitations and improvements

Deviations have been observed regarding both, the stem bending and resulting forces, compared to the reference experiment for the longest stem ($L_s = 0.25$ m) for both material types. One explanation could be the comparably high grid uncertainty (cf. Appendix A.2) that was calculated for the 0.25 m stem (on average 10.42 %) in contrast to the 0.05 m stem (on average 2.39 %) for the intermediate cell size of 1.5×10^{-3} m (see Table A.3). Therefore, a refined cell size would be more accurate for modeling the flow close to the surface of the structure and lead potentially to less deviation in the solution but comes with a high computational cost.

Another explanation could be related to a limitation of the coupled numerical model, which is neglecting any wall shear or skin friction of the stem. With longer stem lengths and corresponding larger surface areas that limitation would be increasingly relevant, in agreement with the presented results of this study, as displayed in Fig. 12 and Fig. 13. For the short stem, the bending is minimal, and compression flow dominates, while the deflected curvature of the long stem results in a much longer stem surface exposed to shear stresses. Correspondingly, the current acting on the upper part of the stem changes from a compression towards a longitudinal shear flow. Wall or skin friction, while increasing the resulting force in one-way coupled approaches, could affect the surrounding hydrodynamics, dissipate energy, and reduce flow velocities, by inducing small-scale turbulence along the surface of the stem. The absence of this process within the presented model is a potential source of error. Gosselin (2019) discussed that the influence of the skin friction for flexible vegetation could be larger for smaller values of Re, which corresponds to the deviations displayed

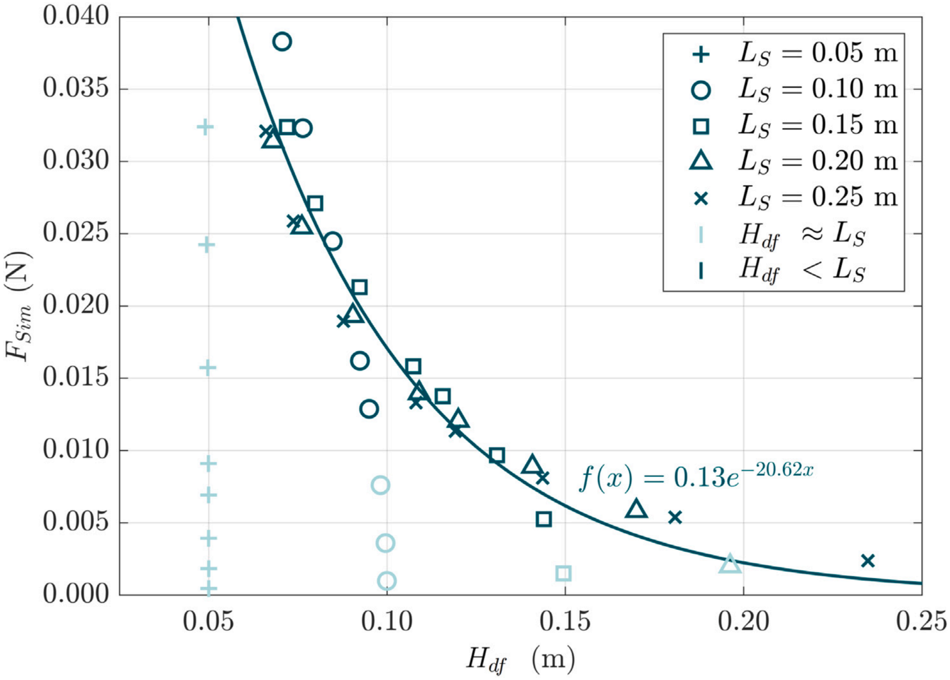

Fig. 18. Relation between simulated forces of the HDPE material to the deflected stem height, including a fitted curve for $H_{df} < L_S$, with the sum of squared errors (SSE) = 0.0002 and $R^2 = 0.93$.

in Fig. 11. Then again, the skin friction might become relevant when the stem is bent parallel to the flow, which is expected for higher current velocities, corresponding to higher values of Re. Future work should therefore integrate skin friction and investigate its influence along the stem. A possible solution to include the vegetation is the application of wall-adapted velocity functions for the coupling of the FSI. Another possibility could be the application of skin friction coefficients to the coupling of the FSI. In the literature (Abdelrhman, 2007; Zhu et al., 2020), a relationship between Re and the skin friction coefficient (C_f) has been applied ($C_f = 0.074Re^{-1/5}$) to simulate flexible vegetation, leading to skin friction coefficients of 0.02, 0.07, and 0.10 (Abdelrhman, 2007; Zeller et al., 2015; Luhar and Nepf, 2016).

The structural solver currently approximates vegetation by a uniform beam of square cross-section; this could be an over-simplification of live vegetation. Field investigations on vegetation have reported a variation of material properties over the plant height, i.e., the diameter or Young's modulus (Keimer et al., 2023). Previous numerical simulations have shown that using uniform properties instead of a variation of material properties over the vegetation height leads to errors predicting the drag coefficient of up to 26 % (Marjoribanks and Paul, 2021). Recently, an approach to include a varying width over the stem height for a Cosserat rod solver has been proposed (Schoppmann et al., 2021); however, the integration of further geometrical properties of plants, like leaves, would require additional modifications currently unaccounted for. More accurately modeled plant configurations, including nodes and leaves, could be of importance, as wave attenuation in field conditions is correlated to leaf properties (Zhang et al., 2022); however, the same correlation could not be observed for the leaf lengths, potentially due to the reconfiguration of longer leaves. Nevertheless, as observed by Keimer et al. (2023), vegetation species in dormancy often lose their leaves, wherefore a beam seems to be a suitable simplification to simulate conditions during storm surge season.

5. Conclusion

When quantitatively assessing the ecosystem services provided by coastal vegetation, such as salt marsh or seagrass, the use of accurate numerical models that adopt a direct forcing approach without reliance on coefficients like C_D enable further evaluation of the involved dynamic processes. Parameters such as the dynamic fluctuation of the current-induced stem motion and the resulting turbulence intensity provide insights regarding the sediment mobility solution around flexible stems. Already recognized as a promising approach, the FSI within the model REEF3D::CFD was evaluated towards its ability to accurately simulate the motion and resulting forces of flexible vegetation under varying current conditions. The specific objectives posed at the beginning of this work could now be addressed as follows:

- The convergence analysis of the structural solver underscores the importance of a fine grid resolution in the proximity of the vegetation stem. In the context of the currents examined in this study, no discernible sensitivity to temporal resolution was observed. For the simulated stem with a length of 0.25 m, an optimal number of individual rigid elements has been determined, totaling 200 elements per meter.

- A comparative assessment of simulated forces employing three turbulence models, namely RANS, URANS and LES, highlighted that the wall-adapted RANS approach represents a more reasonable FSI compared to the non-adapted approach, while the utilization of LES shows the smallest deviations of simulated to experimental forces.
- The outcomes of this investigation demonstrate that the FSI implemented in REEF3D::CFD can accurately replicate both stem bending and associated forces across diverse stem lengths, current velocities, and material compositions.
- The influence of the damping coefficients on the flexible motion of the longer stems under current load was highlighted with a force amplitude spectrum.

Subsequent investigations should prioritize the incorporation of wave conditions and evaluate potential material dependencies of damping coefficients. Addressing the current limitations of the structural solver may involve the inclusion of vegetation skin friction and the variation of material properties along the stem height.

CRediT authorship contribution statement

Inga Prüter: Writing – original draft, Visualization, Validation, Methodology, Formal analysis. **Felix Spröer:** Writing – review & editing, Visualization, Validation, Methodology. **Kara Keimer:** Writing – review & editing, Methodology, Conceptualization. **Oliver Lojek:** Writing – review & editing, Project administration, Methodology, Conceptualization. **Christian Windt:** Writing – review & editing, Validation, Methodology, Conceptualization. **David Schürenkamp:** Writing – review & editing, Methodology, Funding acquisition, Conceptualization. **Hans Bihs:** Methodology, Software, Writing – review & editing. **Ioan Nistor:** Writing – review & editing, Supervision, Methodology, Conceptualization. **Nils Goseberg:** Writing – review & editing, Supervision, Resources, Project administration, Methodology, Funding acquisition, Conceptualization.

Declaration of competing interest

The authors declare that they have no known competing financial interests or personal relationships that could have appeared to influence the work reported in this paper.

Acknowledgments

The authors are grateful Dr. Mihul Luhar and Dr. Silvio Tschisgale provided their research data and also thank Dr. Tobias Martin for his helpful comments on the implementation of the FSI solver in REEF3D code. This work used the supercomputer Phoenix supported by the Gauß-IT-Zentrum of the Technische Universität Braunschweig (GITZ), Germany.

Funding

This study was performed as part of the joint research project “Gute Küste Niedersachsen” funded by the Lower-Saxon Ministry of Research and Culture (FKZ: 76251-17-5/19) and the Volkswagen Stiftung. Open Access funding was enabled and organized by Projekt DEAL.

Appendix A. Model sensitivity

This appendix focuses on the sensitivity analysis of the model regarding the temporal and spatial discretization as well as the number of individual rigid elements, of which the stem consists of.

A.1. Influence of the flume width

First, the influence of the wall on the horizontal flow velocity is investigated. Ensuring computability required a reduction of the experimental flume width of 0.38 m (for the lower current velocities) and 0.76 m (for the higher current velocities). Therefore the time-averaged horizontal velocity of approximately the last six seconds of the simulation in seven flume widths, ranging from 0.08 m to 0.32 m, are compared at four different locations in the flume. Additionally, the influence of using a slip boundary condition for the walls has been tested for the flume width of 0.16 m. Three probes are located in between the inflow and the stem to evaluate the flow conditions acting on the stem and determine the influence of the wall in x- and z-direction. A fourth probe is located in between the stem and the wall to evaluate the wall influence in y-direction, an overview of the positioning of the line probes is given in Fig. 2. The results are visualized in Fig. A.19, where Fig. A.19a displays the inflow boundary condition, which is not yet influenced by the flume width. In Fig. A.19b, c, and d, the influence of the walls is apparent for two flume widths of 0.08 m and 0.12 m.

To quantify the wall influence, the deviation of the depth-averaged horizontal velocity to the widest simulated flume is calculated and displayed in Fig. A.20a. In Fig. A.20b, the deviation of the average simulated force compared to the average simulated force of the widest tested flume is displayed. Additionally, the simulation time for each flume width is visualized. As the deviation of the horizontal velocity for the flume width of 0.16 m is at about 2 % and of about 3 % for the average force, while simulating twice as fast as the 0.32 m wide flume, it is a reasonable compromise between results' accuracy and simulation time. The slip BC was not chosen, as it can be seen in Fig. A.19 in that the flow profile deviates from the other no-slip boundary conditions cases still at the lower height of the tip, thus leading to potentially different results compared to those from the physical experiments. The ideal combination could be in conclusion a no-slip BC for the bottom of the flume and a slip BC for the flume walls. However, this possibility is currently not implemented in the used finite-differences solver.

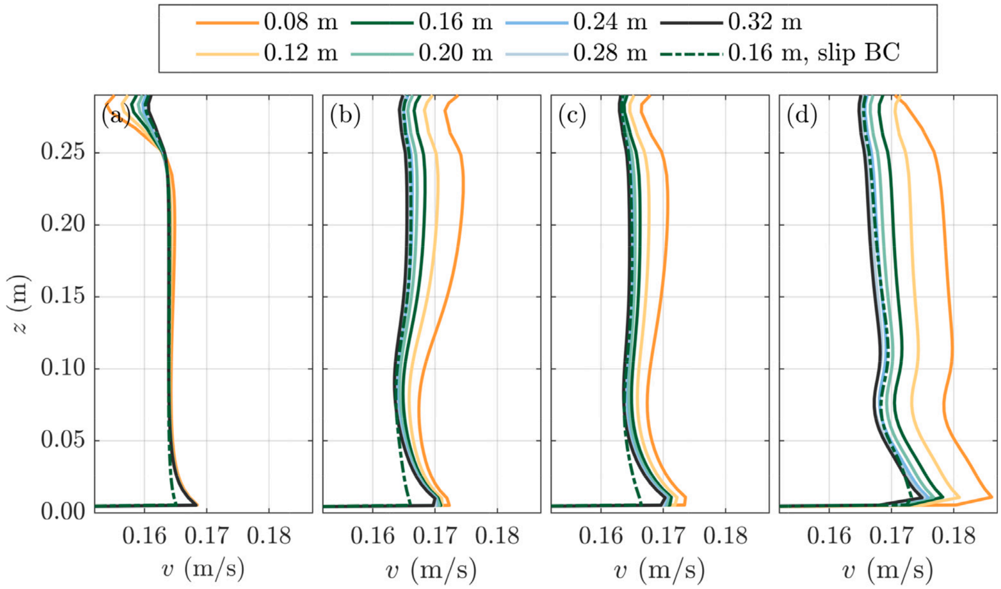

Fig. A.19. Comparison of the time-averaged horizontal velocity for a variation of flume widths, for (a) Probe 1 at $x = 0.025$, $y = 0.00$, (b) Probe 2 at $x = 0.05$, $y = 0.00$, (c) Probe 3 at $x = 0.075$, $y = 0.00$ and (d) Probe (4) at $x = 0.15$, $y = 0.03$.

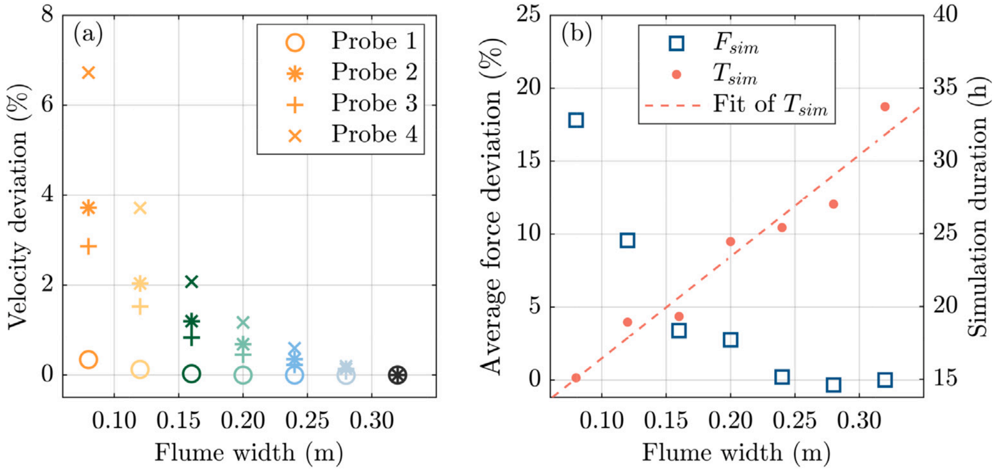

Fig. A.20. Comparison of (a) the deviation of the horizontal velocity to the horizontal velocity of the widest simulated flume and (b) the deviation of the simulated force to the simulated force of the widest simulated flume, including the simulation duration for a variation of flume widths.

A.2. Grid convergence study

A grid convergence study has been carried out for both materials used in the experiments to be able to determine the necessary grid resolution to reproduce the forces acting on the stem, following Cummins et al. (2017), based on the assumption:

$$\phi(h) = \phi_0 + \alpha h^p \tag{A.1}$$

Here, h_i corresponds to the ratio of the cell sizes of the ith grid to that of the reference grid and ϕ_i to the ratio of simulated forces to the force of the reference grid. For each material type and stem length, quadratic convergence is assumed, making p equal to two. Correspondingly, a parabola is applied for the curve fit to evaluate ϕ_0, which describes the estimated normalized force in the limit of infinite resolution. The parameters ϕ_0 and α are then obtained by the least squares method. Afterwards, the standard error of the fit is calculated by

$$\sigma_{fit} = \sqrt{\frac{\sum_{i=1}^{n_g} (\phi_i - \phi(h_i))^2}{n}}, \tag{A.2}$$

Table A.3
Grid convergence after (Cummins et al., 2017) for the HDPE and soft foam material with $v = 0.16$ m/s.

Material	Refined cell size	$L_S = 0.05$ m		$L_S = 0.25$ m	
		Drag force	Grid uncertainty	Drag forces	Grid uncertainty
–	(m)	(N)	%	(N)	%
	0.75×10^{-3}	0.0089	1.48	0.0127	2.43
HDPE	1.5×10^{-3}	0.0091	3.31	0.0133	8.06
	3.0×10^{-3}	0.0093	6.05	0.0159	32.50
	0.75×10^{-3}	0.0074	1.47	0.0125	2.65
Soft foam	1.5×10^{-3}	0.0074	1.47	0.0136	12.77
	3.0×10^{-3}	0.0077	6.53	0.0162	36.66

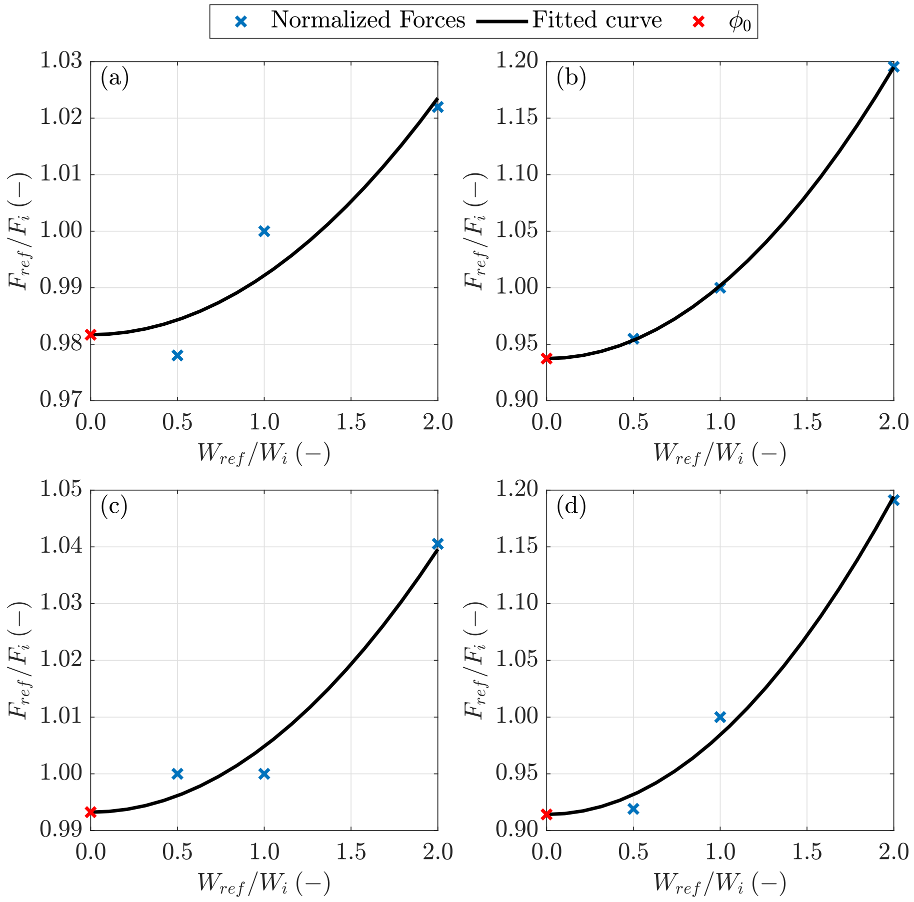

Fig. A.21. Grid convergence study after Cummins et al. (2017) for grid sizes in the refined area of 0.75×10^{-3} m, 1.5×10^{-3} m and 3.0×10^{-3} m for (a) the 0.05 m and (b) the 0.25 m-long HDPE stem as well as (c) the 0.05 m and (d) the 0.25 m-long soft foam stem.

including $n = n_g - 3$ as the number of degrees of freedom of the fit. Additionally, the error of the reference grid is estimated by $\delta = |1 - \phi_0|$. The grid uncertainty is then calculated including a safety factor of 1.25 and the standard error of the fit.

$$U_g = 1.25\delta + \sigma_{fit} \tag{A.3}$$

The calculated grid uncertainties are summarized in Table A.3. The resulting regressions for two material types and stem lengths are visualized in Fig. A.21.

Table A.4
Simulated drag force (F_{sim}) for two different test cases with varying CFL-criteria (0.2 - 1.0) and the time in hours required to simulate 20.0 s.

CFL-criterion (-)	HDPE, v = 0.16 m/s, L_S = 0.05 m		SF, v = 0.32 m/s, L_S = 0.25 m	
	F_{sim} (N)	Time (h)	F_{sim} (N)	Time (h)
0.2	0.0093	216	0.0220	329
0.4	0.0091	106	0.0224	171
0.6	0.0091	72	0.0222	122
0.8	0.0092	53	0.0222	88
1.0	0.0091	47	0.0224	70

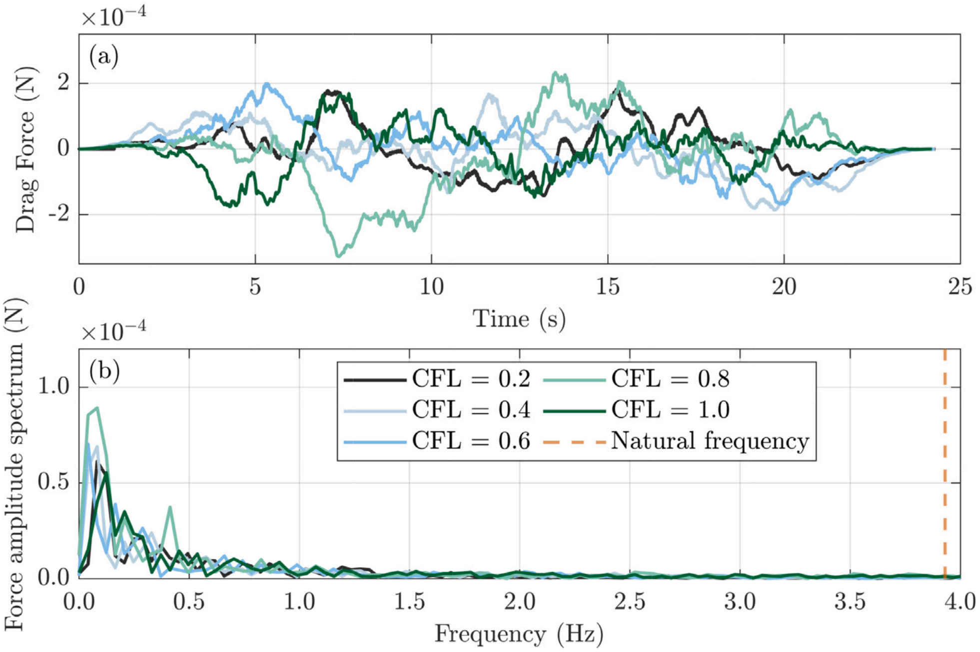

Fig. A.22. Comparison of the simulated forces for a variation of CFL-criterions by transferring the data from (a) the time series to (b) the frequency domain for the HDPE stem with v = 0.16 m/s, L_S = 0.05 m, including the natural frequency of the stem.

A.3. Influence of the CFL-criterion

In the fluid solver, the time step size is calculated based on the Courant– Friedrichs–Lewy (CFL)-criterion. To test the model sensitivity, the CFL-criterion has been varied for the 0.05 m long HDPE stem with a medium current velocity (0.16 m/s) and the 0.25 m long soft foam stem with a high current velocity (0.32 m/s). The resulting forces are shown in Table A.4, with results differing by a maximum of 2.12 % for the HDPE material relative to the simulated results with the lowest CFL-criterion.

In addition, the time series of the forces has been evaluated, corresponding to the evaluation of the damping coefficients, and compared in the frequency spectrum. Additionally, the natural frequency of the stem has been calculated based on Eq. (14). The results, shown in Fig. A.22, suggest that the CFL-criterion has a minor influence on the fluctuations of the simulated forces. For the satisfactory convergence of drag forces involving uniform current conditions, the CFL-criterion is set equal to unity, which additionally reduces the simulation duration.

A.4. Choice of number of elements

The stem movement and resulting forces exerted on the 0.25 m stem have been tested for varying numbers of elements (n = 5 to 100), the results are shown in Fig. A.23. Depending on the degree of curvature, more elements are required to reproduce the bending of the physical stem correctly, as shown in Fig. A.23a and b. The sharpest curvature appears for the 0.25 m long soft foam stem with the highest current velocity of 0.32 m/s. To quantify the accuracy of the stem bending in relation to the physical results, the RMSE is additionally calculated. With a lower number of elements (n = 5 to 20), large differences in the resulting bending of the stem can be seen (cf. Fig. A.23d). In contrast, the results remain similar for the larger number of elements (n = 25, 50, 100). Correspondingly, the largest variation of the resulting forces is observed for element numbers smaller than 25 and stays relatively constant afterward, for both tested materials (cf. Fig. A.23c).

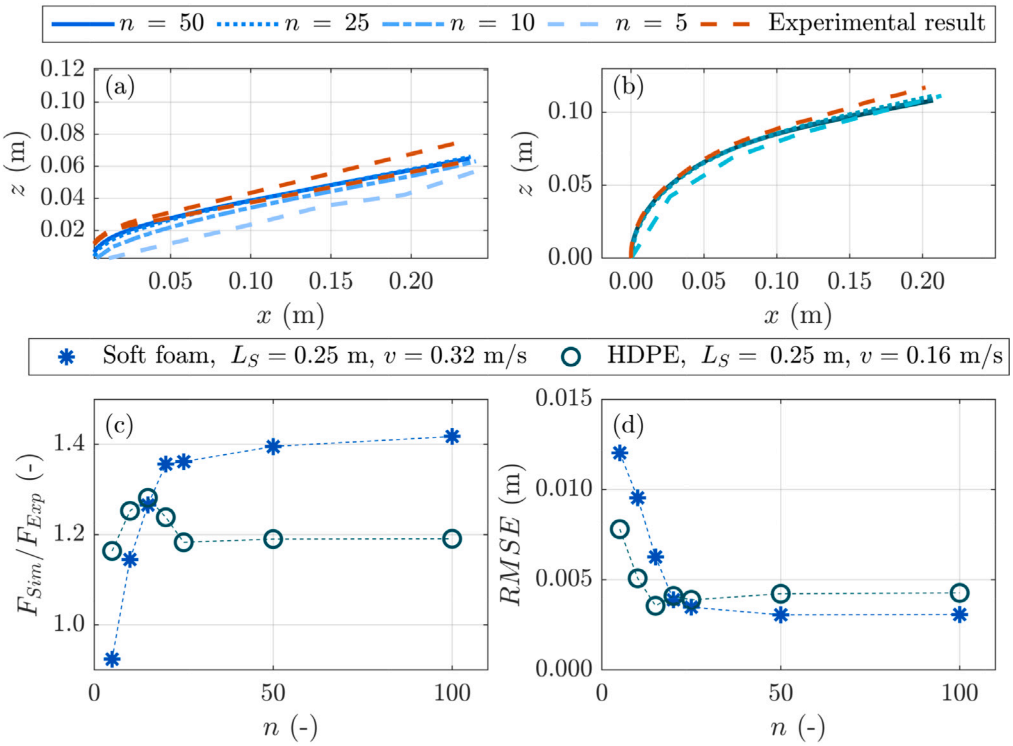

Fig. A.23. Variation of the number of elements for the simulated stem and comparison to the experimental data of Luhar and Nepf (2011) with (a) visualization of the bending behavior for soft foam material and $v = 0.32\,\mathrm{m/s}$ for a selected number of elements, (b) visualization of the bending behavior for the HDPE material and $v = 0.16\,\mathrm{m/s}$ for a selected number of elements, (c) visualization of the normalized forces and (d) the root-mean-square error (RMSE) for the bending behavior for both materials.

Table A.5
Number of elements for the different stem lengths.

Stem length L_S (m)	No. of elements n –	No. of elements per meter (n/m)	Length per element (m/n)
0.05	20	400	2.5×10^{-3}
0.10	32	320	3.6×10^{-3}
0.15	40	267	4.3×10^{-3}
0.20	46	230	4.7×10^{-3}
0.25	50	200	5.0×10^{-3}

Therefore, 50 elements, equivalent to $200\,\mathrm{n/m}$, are chosen for the $0.25\,\mathrm{m}$ stem, given that the computational time also increases with increasing number of elements. For the $0.05\,\mathrm{m}$ stem, it has been observed that the solver diverges when using $200\,\mathrm{n/m}$, leading to unstable simulations for faster current velocities. Increasing the number of elements to 20 ($400\,\mathrm{n/m}$) stabilized the simulations for the shortest stem. With the number of elements set to $400\,\mathrm{n/m}$ for the $0.05\,\mathrm{m}$ long stem and $200\,\mathrm{n/m}$ for the $0.25\,\mathrm{m}$ long stem, the number of elements for the remaining stem lengths have been selected accordingly, with a linear increase in the length per element, as detailed in Table A.5 in the appendix.

Data availability

Data will be made available on request.

References

Abdelrhman, M.A., 2007. Modeling coupling between eelgrass zostera marina and water flow. Mar. Ecol. Prog. Ser. 338, 81–96. http://dx.doi.org/10.3354/meps338081.

Agrawal, V., Kulachenko, A., Scapin, N., Tammisola, O., Brandt, L., 2024. An efficient isogeometric/finite-difference immersed boundary method for the fluid–structure interactions of slender flexible structures. Comput. Methods Appl. Mech. Engrg. 418, http://dx.doi.org/10.1016/j.cma.2023.116495.

Anderson, M., Smith, J., 2014. Wave attenuation by flexible, idealized salt marsh vegetation. Coast. Eng. 83, 82–92. http://dx.doi.org/10.1016/j.coastaleng.2013.10.004.

Bihs, H., Kamath, A., Alagan Chella, M., Aggarwal, A., Arntsen, Ø., 2016. A new level set numerical wave tank with improved density interpolation for complex wave hydrodynamics. Comput. & Fluids 140, 191–208. http://dx.doi.org/10.1016/j.compfluid.2016.09.012.

Bouma, T.J., Vries, M.B.d., Low, E., Peralta, G., Tánczos, I.C., van de Koppel, J., Herman, P.M.J., 2005. Trade-offs related to ecosystem engineering: A case study on stiffness of emerging macrophytes. Ecology 86 (8), 2187–2199. http://dx.doi.org/10.1890/04-1588.

Bush, R.H., Chyczewski, T.S., Duraisamy, K., Eisfeld, B., Rumsey, C.L., Smith, B.R., 2019. Recommendations for future efforts in RANS modeling and simulation. Paper presented at the AIAA Scitech 2019 Forum, in San Diego, California, 7–11 January 2019.

Caroppi, G., Järvelä, J., 2022. Shear layer over floodplain vegetation with a view on bending and streamlining effects. Environ. Fluid. Mech. 22 (2-3), 587–618. http://dx.doi.org/10.1007/s10652-022-09841-w.

Chen, H., Zou, Q.-P., 2019. Eulerian–Lagrangian flow-vegetation interaction model using immersed boundary method and OpenFOAM. Adv. Water Resour. 126, 176–192. http://dx.doi.org/10.1016/j.advwatres.2019.02.006.

Chourdakis, G., Schneider, D., Uekermann, B., 2023. Openfoam-precice: Coupling openfoam with external solvers for multi-physics simulations. OpenFOAM J. 3, 1–25. http://dx.doi.org/10.51560/ofj.v3.88.

Cui, T., He, G., Jiang, M., Wang, W., Yuan, L., Han, D., Kamath, A., Bihs, H., 2022a. Large eddy simulation of focused breaking waves with different wave steepness. Ocean Model. 179, http://dx.doi.org/10.1016/j.ocemod.2022.102122.

Cui, T., Kamath, A., Wang, W., Han, D., Bihs, H., 2022b. Large-eddy simulations of gravity currents in the presence of waves. J. Hydraul. Res. 60:5, 770–791. http://dx.doi.org/10.1080/00221686.2022.2064345.

Cummins, C., Viola, I.M., Mastropaolo, E., Nakayama, N., 2017. The effect of permeability on the flow past permeable disks at low Reynolds numbers. Phys. Fluids 29 (9), http://dx.doi.org/10.1063/1.5001342.

Dijkstra, J.T., Uittenbogaard, R.E., 2010. Modeling the interaction between flow and highly flexible aquatic vegetation. Water Resour. Res. 46, http://dx.doi.org/10.1029/2010WR009246.

el Rahi, J., Martínez-Estévez, I., Tagliafierro, B., Domínguez, J., Crespo, A., Stratigaki, V., Suzuki, T., Troch, P., 2023. Numerical investigation of wave-induced flexible vegetation dynamics in 3D using a coupling between DualSPHysics and the FEA module of project chrono. Ocean Eng. 285, http://dx.doi.org/10.1016/j.oceaneng.2023.115227.

Ferziger, J.H., Perić, M., 2002. Computational Methods for Fluid Dynamics. Springer Berlin, Heidelberg.

Freund, J., Karakoç, A., 2016. Shear and torsion correction factors of timoshenko beam model for generic cross sections. Res. Eng. Struct. Mat. http://dx.doi.org/10.17515/resm2015.19me0827.

Gosselin, F.P., 2019. Mechanics of a plant in fluid flow. J. Exper. Botany 70 (14), 3533–3548. http://dx.doi.org/10.1093/jxb/erz288.

Hagmeyer, N., Mayr, M., Popp, A., 2024. A fully coupled regularized mortar-type finite element approach for embedding one-dimensional fibers into three-dimensional fluid flow. Numer. Meth Eng. 125 (8), http://dx.doi.org/10.1002/nme.7435.

He, S., Liu, H., Shen, L., 2022. Simulation-based study of turbulent aquatic canopy flows with flexible stems. J. Fluid Mech. 947, http://dx.doi.org/10.1017/jfm.2022.655.

Himes-Cornell, A., Pendleton, L., Atiyah, P., 2018. Valuing ecosystem services from blue forests: A systematic review of the valuation of salt marshes, sea grass beds and mangrove forests. Ecosyst. Serv. 30, Part A, 36–48. http://dx.doi.org/10.1016/j.ecoser.2018.01.006.

Huai, W.-x., Zhang, J., Katul, G.G., Cheng, Y.-g., Tang, X., Wang, W.-j., 2019. The structure of turbulent flow through submerged flexible vegetation. J. Hydrodyn. 31 (2), 274–292. http://dx.doi.org/10.1007/s42241-019-0023-38.

Jin, C., Zhang, J., 2022. Numerical investigation of the wave interaction with flexible vegetation: model setup and validation for a single stem study case. Anthropocene Coast. 5, http://dx.doi.org/10.1007/s44218-022-00003-5.

Katopodes, N.D., 2019. Free-surface flow. Environmental fluid mechanics. Butterworth-Heinemann, Oxford.

Keimer, K., Kind, F., Prüter, I., Kosmalla, V., Lojek, O., Schürenkamp, D., Prinz, M., Niewerth, S., Aberle, J., Goseberg, N., 2024. From seasonal field study to surrogate modeling: Investigating the biomechanical dynamics of elymus sp. in salt marshes. Limnograp. Oceanograph. Methods http://dx.doi.org/10.1002/lom3.10616.

Keimer, K., Kosmalla, V., Prüter, I., Lojek, O., Prinz, M., Schürenkamp, D., Freund, H., Goseberg, N., 2023. Proposing a novel classification of growth periods based on biomechanical properties and seasonal changes of spartina anglica. Front. Mar. Sci. 10, http://dx.doi.org/10.3389/fmars.2023.1095200.

Kim, H.D., Yu, X., Kaplan, D., 2024. Steady flow over a finite patch of submerged flexible vegetation. Water Resour. Res. 60 (1), http://dx.doi.org/10.1029/2023WR035222.

King, S., Lester, J., 1995. The value of salt marsh as a sea defence. Marine Poll. Bull. 30, 180–189.

Lang, H., Linn, J., Arnold, M., 2011. Multi-body dynamics simulation of geometrically exact cosserat rods. Multibody Syst. Dyn. 25 (3), 285–312. http://dx.doi.org/10.1007/s11044-010-9223-x.

Le Bouteiller, C., Venditti, J.G., 2015. Sediment transport and shear stress partitioning in a vegetated flow. Water Resour. Res. 51 (4), 2901–2922. http://dx.doi.org/10.1002/2014WR015825.

Linn, J., Lang, A., 2013. Geometrically exact cosserat rods with Kelvin–Voigt type viscous damping. Mech. Sci. 4 (1), 79–96. http://dx.doi.org/10.5194/ms-4-79-2013.

Liu, J., Kutschke, S., Keimer, K., Kosmalla, V., Schürenkamp, D., Goseberg, N., Böl, M., 2021. Experimental characterisation and three-dimensional modelling of elymus for the assessment of ecosystem services. Ecol. Eng. 166, http://dx.doi.org/10.1016/j.ecoleng.2021.106233.

Liu, C., Yan, C., Sun, S., Lei, J., Nepf, H., Shan, Y., 2022. Velocity, turbulence, and sediment deposition in a channel partially filled with a phragmites australis canopy. Water Resour. Res. 58 (8), http://dx.doi.org/10.1029/2022WR032381.

Losada, I.n.J., Maza, M., Lara, J.L., 2016. A new formulation for vegetation-induced damping under combined waves and currents. Coast. Eng. 107, 1–13. http://dx.doi.org/10.1016/j.coastaleng.2015.09.011.

Lou, S., Wang, H., Liu, H., Zhong, G., Radnaeva, L.D., Nikitina, E., Ma, G., Liu, S., 2021. Laboratory study of the effects of flexible vegetation on solute diffusion in unidirectional flow. Environ. Sci. Eur. 33 (1), http://dx.doi.org/10.1186/s12302-021-00521-y.

Luhar, M., Nepf, H.M., 2011. Flow-induced reconfiguration of buoyant and flexible aquatic vegetation. Limnol. Oceanogr. 56, 2003–2017. http://dx.doi.org/10.4319/lo.2011.56.6.2003.

Luhar, M., Nepf, H.M., 2016. Wave-induced dynamics of flexible blades. J. Fluids Struct. 61, 20–41. http://dx.doi.org/10.1016/j.jfluidstructs.2015.11.007.

Marin-Diaz, B., van der Wal, D., Kaptein, L., Martinez-Garcia, P., Lashley, C.H., Jong, K.d., Nieuwenhuis, J.W., Govers, L.L., Olff, H., Bouma, T.J., 2023. Using salt marshes for coastal protection: Effective but hard to get where needed most. J. Appl. Ecol. http://dx.doi.org/10.1111/1365-2664.14413.

Marjoribanks, T.I., Paul, M., 2021. Modelling flow-induced reconfiguration of variable rigidity aquatic vegetation. J. Hydraul. Res. 1–6. http://dx.doi.org/10.1080/00221686.2020.1866693.

Martin, T., Bihs, H., 2021. A numerical solution for modelling mooring dynamics, including bending and shearing effects, using a geometrically exact beam model. JMSE 9 (5), 486. http://dx.doi.org/10.3390/jmse9050486.

Mattis, S.A., Dawson, C.N., Kees, C.E., Farthing, M.W., 2015. An immersed structure approach for fluid-vegetation interaction. Adv. Water Resour. 80, http://dx.doi.org/10.1016/j.advwatres.2015.02.014.

Maza, M., Lara, J.L., Losada, I.J., 2013. A coupled model of submerged vegetation under oscillatory flow using Navier–Stokes equations. Coast. Eng. 80, 16–34. http://dx.doi.org/10.1016/j.coastaleng.2013.04.009.

Mullarney, J.C., Henderson, S.M., 2010. Wave-forced motion of submerged single-stem vegetation. J. Geophys. Res. 115, http://dx.doi.org/10.1029/2010JC006448.

Ni, J., Ji, C., Xu, D., Zhang, X., Liang, D., 2023. On monami modes and scales of a flexible vegetation array in a laminar boundary layer. Phys. Fluids 35 (7), http://dx.doi.org/10.1063/5.0155506.

Nicoud, F., Ducros, F., 1999. Subgrid-scale stress modelling based on the square of the velocity gradient tensor.. Flow Turbul. Combust. 62, 183–200.

O'Connor, J., Rogers, B.D., 2021. A fluid-structure interaction model for free-surface flows and flexible structures using smoothed particle hydrodynamics on a GPU. J. Fluids Struct. 104, http://dx.doi.org/10.1016/j.jfluidstructs.2021.103312.

Ondiviela, B., Losada, I.J., Lara, J.L., Maza, M., Galván, C., Bouma, T.J., van Belzen, J., 2014. The role of seagrasses in coastal protection in a changing climate. Coast. Eng. 87, 158–168. http://dx.doi.org/10.1016/j.coastaleng.2013.11.005.

Ouro, P., Stoesser, T., 2017. An immersed boundary-based large-eddy simulation approach to predict the performance of vertical axis tidal turbines. Comput. Fluids 152, 74–87. http://dx.doi.org/10.1016/j.compfluid.2017.04.003.

Puijalon, S., Bouma, T.J., Douady, C.J., van Groenendael, J., Anten, N.P.R., Martel, E., Bornette, G., 2011. Plant resistance to mechanical stress: evidence of an avoidance-tolerance trade-off. New Phytol. 191 (4), 1141–1149. http://dx.doi.org/10.1111/j.1469-8137.2011.03763.x.

Rupprecht, F., Möller, I., Paul, M., Kudella, M., Spencer, T., van Wesenbeeck, B.K., Wolters, G., Jensen, K., Bouma, T., Miranda-Lange, M., Schimmels, S., 2017. Vegetation-wave interactions in salt marshes under storm surge conditions. Ecol. Eng. 100, 301–315. http://dx.doi.org/10.1016/j.ecoleng.2016.12.030.

Sasikumar, A., Kamath, A., Bihs, H., 2020. Modeling porous coastal structures using a level set method based VRANS-solver on staggered grids. Coastal Eng. J. 62 (2), 198–216. http://dx.doi.org/10.1080/21664250.2020.1734412.

Schoppmann, K., Löhrer, B., Tschisgale, S., Fröhlich, J., Langre, E.d., 2021. An efficient solver for a cosserat rod of non-constant width applied to a problem of fluid-structure interaction. Proc. Appl. Math. Mech. 21 (1), http://dx.doi.org/10.1002/pamm.202100152.

Tian, F.-B., Dai, H., Luo, H., Doyle, J.F., Rousseau, B., 2014. Fluid-structure interaction involving large deformations: 3D simulations and applications to biological systems. J. Comput. Phys. 258, http://dx.doi.org/10.1016/j.jcp.2013.10.047.

Tschisgale, S., Fröhlich, J., 2020. An immersed boundary method for the fluid-structure interaction of slender flexible structures in viscous fluid. J. Comput. Phys. 423 (7), http://dx.doi.org/10.1016/j.jcp.2020.109801.

Tschisgale, S., Löhrer, B., Meller, R., Fröhlich, J., 2021. Large eddy simulation of the fluid–structure interaction in an abstracted aquatic canopy consisting of flexible blades. J. Fluid Mech. 916, http://dx.doi.org/10.1017/jfm.2020.858.

van Veelen, T.J., Fairchild, T.P., Reeve, D.E., Karunarathna, H., 2020. Experimental study on vegetation flexibility as control parameter for wave damping and velocity structure. Coast. Eng. 157, http://dx.doi.org/10.1016/j.coastaleng.2020.103648.

Vuik, V., Borsje, B.W., Willemsen, P.W., Jonkman, S.N., 2019. Salt marshes for flood risk reduction: Quantifying long-term effectiveness and life-cycle costs. Ocean Coastal Manag. 171, 96–110. http://dx.doi.org/10.1016/j.ocecoaman.2019.01.010.

Wang, M., Avital, E.J., Bai, X., Ji, C., Xu, D., Williams, J.J.R., Munjiza, A., 2020. Fluid–structure interaction of flexible submerged vegetation stems and kinetic turbine blades. Comp. Part. Mech. 7 (5), http://dx.doi.org/10.1007/s40571-019-00304-6.

Wang, J., He, G., Dey, S., Fang, H., 2022. Influence of submerged flexible vegetation on turbulence in an open-channel flow. J. Fluid Mech. 947, http://dx.doi.org/10.1017/jfm.2022.598.

Whittaker, P., Wilson, C.A., Aberle, J., 2015. An improved Cauchy number approach for predicting the drag and reconfiguration of flexible vegetation. Adv. Water Resour. 83, 28–35. http://dx.doi.org/10.1016/j.advwatres.2015.05.005.

Windt, C., Davidson, J., Ringwood, J., 2021. Investigation of turbulence modeling for point-absorber type wave energy converters. Energies 14 (26), http://dx.doi.org/10.3390/en14010026.

Xu, Z., Shu, C.-W., 2005. Anti-diffusive flux corrections for high order finite difference WENO schemes. J. Comput. Phys. 205 (2), 458–485. http://dx.doi.org/10.1016/j.jcp.2004.11.014.

Zeller, R.B., Zarama, F.J., Weitzman, J.S., Koseff, J.R., 2015. A simple and practical model for combined wave–current canopy flows. J. Fluid Mech. 767, 842–880. http://dx.doi.org/10.1017/jfm.2015.59.

Zhang, X., Lin, P., Nepf, H., 2022. A wave damping model for flexible marsh plants with leaves considering linear to weakly nonlinear wave conditions. Coast. Eng. 175, http://dx.doi.org/10.1016/j.coastaleng.2022.104124.

Zhu, L., Zou, Q.-P., Huguenard, K., Fredriksson, D.W., 2020. Mechanisms for the asymmetric motion of submerged aquatic vegetation in waves: A consistent-mass cable model. J. Geophys. Res. Oceans 125, http://dx.doi.org/10.1029/2019JC015517.